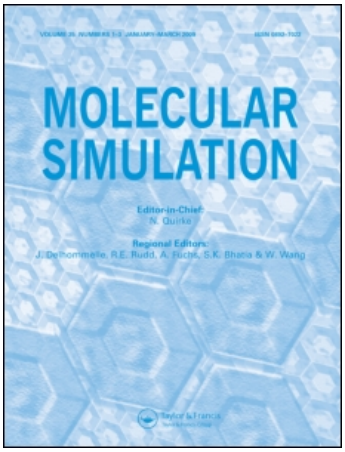

Molecular Simulation
Publication details, including instructions for authors and subscription information:
http://www.informaworld.com/smpp/title~content=t713644482

Conformation, dynamics and ion-binding properties of single-chain polyuronates: a molecular dynamics study

Lovorka Perić[a]; Cristina S. Pereira[a]; Serge Pérez[b]; Philippe H. Hünenberger[a]
[a] Laboratory of Physical Chemistry, ETH-Hönggerberg, Zürich, Switzerland [b] Centre de Recherches sur les Macromolécules Végétales, Grenoble, France

To cite this Article Perić, Lovorka , Pereira, Cristina S. , Pérez, Serge and Hünenberger, Philippe H.(2008) 'Conformation, dynamics and ion-binding properties of single-chain polyuronates: a molecular dynamics study', Molecular Simulation, 34: 4, 421 — 446
To link to this Article: DOI: 10.1080/08927020701759699
URL: http://dx.doi.org/10.1080/08927020701759699

Molecular Simulation
Vol. 34, No. 4, April 2008, 421–446

Taylor & Francis
Taylor & Francis Group

Conformation, dynamics and ion-binding properties of single-chain polyuronates: a molecular dynamics study

Lovorka Perić[a], Cristina S. Pereira[a], Serge Pérez[b] and Philippe H. Hünenberger[a]*

[a]*Laboratory of Physical Chemistry, ETH-Hönggerberg, Zürich, Switzerland;* [b]*Centre de Recherches sur les Macromolécules Végétales, Grenoble, France*

(Received 21 October 2007; final version received 29 October 2007)

In the present study, we report and compare sixteen explicit-solvent molecular dynamics simulations (10 ns) of homopolyuronate single chains corresponding to poly-β(1 → 4)-D-glucuronate (pGlcU), poly-β(1 → 4)-D-mannuronate (pManU), poly-α(1 → 4)-D-galacturonate (pGalU) and poly-α(1 → 4)-L-guluronate (pGlcU). Eight main simulations are performed at 300 K in the presence of Ca^{2+} counter-ions (neutralising amount), and starting from alternative regular two- and three-fold helical structures. Eight simulation variants probe the effect of an elevated temperature or of a different counter-ion environment. The chains are made formally infinite by application of artificial periodicity along the chain axis (octameric or nonameric repeat unit). The main observations made in these simulations are: (i) the glycosidic linkages (and local helical parameters) show an important flexibility (in time) and variability (along the chains), and regular helical structures only account for a limited fraction of the conformational ensembles populated at 300 K; (ii) for all system considered, the binding of Ca^{2+} counter-ions is essentially non-specific, with the formation of a dense counter-ion atmosphere around the chains (condensation), but no specific (tight-binding) interactions at well-defined coordination sites; (iii) the 3_2-, 9_5-, 2_1- and 2_1-helices appear to be the preferential regular helical forms for single chain pGlcU, pManU, pGalU and pGulU, respectively, in aqueous solution, with the possibility of a 3_1-helix for pGalU (these forms should be viewed in the sense of helical propensities). Taken together, these observations suggest that if chain dimers are appropriately described by the egg-box model (or any other structural model with similar qualitative features) chain–chain association within junction zones in gels must be accompanied by a substantial chain stiffening and a dramatic change in the ion-binding mode.

Keywords: computer simulation; molecular dynamics; polyuronates; conformation; ion binding

1. Introduction

Polyuronates [1–4] are (predominantly) polymers of uronic acids in (1 → 4)-linkage (Figures 1 and 2). In aqueous solution and at neutral pH, they are polyelectrolytes due to the ionisation of their acidic groups. These polymers have diverse biological functions in plants, such as the preservation of the structure, texture and flexibility, as well as the prevention of dessiccation [5–9]. These functions are related to their ability to form gels [2–4], typically in the presence of divalent metal cations. The three most important natural derivatives of polyuronates are pectins, alginates and glucuronans.

Pectins [2–4,7–10] present a complex sequence alternating homogenous segments of α-D-galacturonate (α-D-GalU) residues in (1 → 4)-linkage ('smooth regions') and highly-branched segments ('hairy regions') comprising neutral sugar molecules (dominantly rhamnose, galactose, and arabinose). They are present in the cell walls of earth plants (1–2% of the dry weight), and are particularly abundant in fruits and vegetables (10–30%). Pectins may be (methoxy-)esterified to different extents, which strongly influences their physico-chemical properties [11–14] (e.g. solid state structure, solubility and gel formation characteristics).

Alginates [2–4,6–15] are linear copolymers of β-D-mannuronate (β-D-ManU) and α-L-guluronate (α-L-GulU) residues in (1 → 4)-linkage, predominantly alternating homogeneous segments of either types of residues and regular repeats of their dimer [16]. The relative amounts of the two acids and their distribution along the polymer chain varies widely depending on the natural source [6,15], and strongly influences the physico-chemical properties of alginates [6,17]. They are present in large amounts in the extracellular medium of brown seaweeds (20–40% of the dry weight) and, for this reason, constitute the most abundant marine biopolymer.

Finally, glucuronans [18–20] are linear polymers of β-D-glucuronate (β-D-GlcU) in (1 → 4)-linkage.

*Corresponding author. Email: phil@igc.phys.chem.ethz.ch

ISSN 0892-7022 print/ISSN 1029-0435 online

DOI: 10.1080/08927020701759699
http://www.informaworld.com

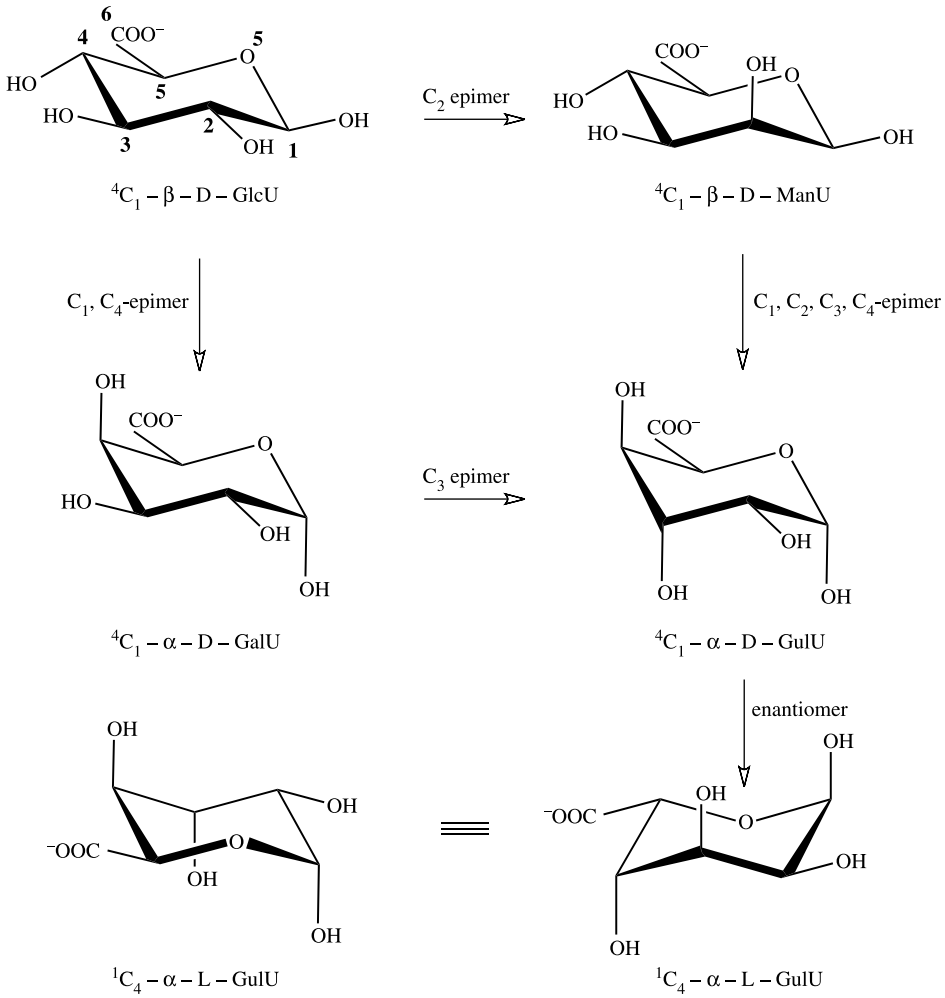

Figure 1. Chemical structures of the four uronate building blocks (β-D-GlcU, β-D-ManU, α-D-GalU and α-L-GulU; anomery representative of the linkage in the corresponding homopolyuronate; Figure 2). All compounds are represented in their most stable ($^4C_1$ or $^1C_4$) chair conformation. The (non-natural) D-enantiomer α-D-GulU is also included (centre right drawing), as well as a non-standard representation of the $^1C_4$-α-L-GulU chair conformation (bottom left drawing). The atom numbering is also indicated (top left drawing).

They are produced by some moulds (as fragments of the more complex heteropolysaccharide mucorane [21]) and strains of bacteria (in a partially acetylated form [18,22]).

The properties of natural polyuronate-based materials are largely used in the food industry, where these polysaccharides serve as stabilisers, thickeners, gelling or emulsifying agents [7,15,23]. In addition, they have found many applications in the fields of medicine (encapsulation, prints), biochemistry (chromatography, culture media), biotechnology (immobilisation of enzymes) and environmental protection (detoxification of industrial wastes) [5,15,24–28]. Most of these industrial and technological applications rest on the ability of polyuronates to form gels [2–4].

An aqueous gel is formed when the polysaccharide chains associate through non-covalent interactions at the level of junction zones. These zones are separated by disordered segments consisting in general of only one chain. The framework of associated and disordered segments leaves large-sized cavities filled by water molecules. In the context of natural pectins and alginates, the size of the junction zones is typically limited by inhomogeneities of two types in the polymer sequence: (i) the presence of destructuring residues, whith a substitution (e.g. methylation or glycosylation) preventing them to enter into a regular structure; (ii) the presence, in a copolymer, of segments with heterogeneous sequences and reduced propensities to chain–chain association. This size limitation of the junction zones prevents the formation of crystalline structures (precipitation) and, consequently, stabilises the polymer–water system in the gel state. The gelation of polyuronates is generally induced by addition of divalent metal cations (typically Ca^{2+}) at a pH close to neutrality.

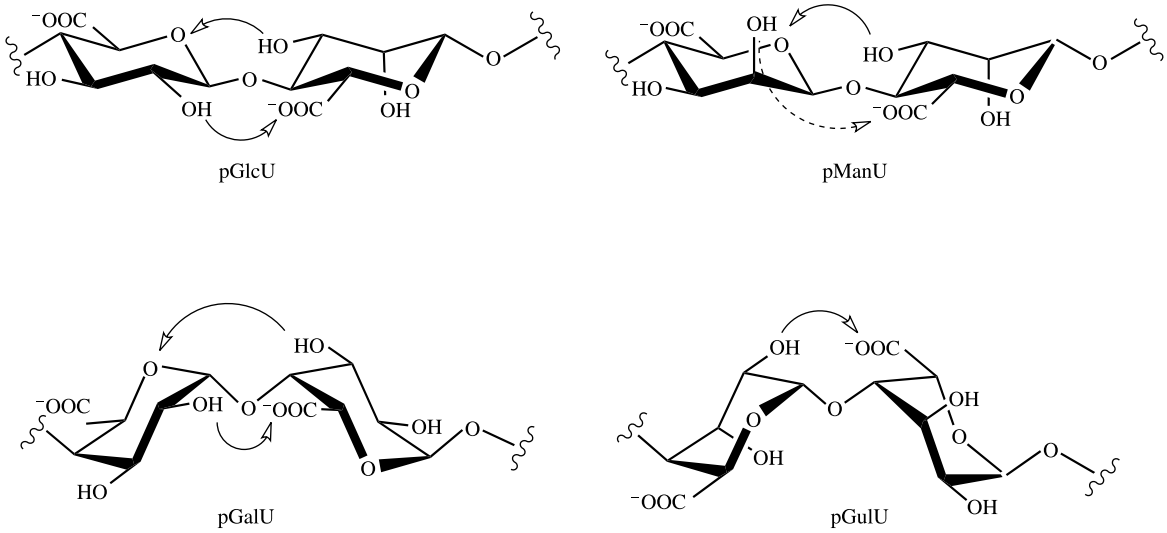

Figure 2. Schematic representations of the linkages found in the four homopolyuronates considered in the present study (poly-β(1 → 4)-D-GlcU, poly-β(1 → 4)-D-ManU, poly-α(1 → 4)-D-GalU and poly-α(1 → 4)-L-GulU; abreviated as pGlcU, pManU, pGalU and pGulU, respectively). The drawings are oriented (left to right) from the non-reducing end to the reducing end. The linkage geometry is chosen to be approximately representative of the one that would be found in a regular a 2-helix. The β(1 → 4) linkage (pGlcU and pManU) is diequatorial (similar to cellulose [101,106]) while the α(1 → 4)-linkage (pGalU and pGulU) is diaxial (similar to amylose [107,108]). Possible inter-residue hydrogen bonds across the glycosidic linkage are indicated by arrows: $H_2 \rightarrow O'_6$ (left to right arrow; O'_6 stands for either or both of the carboxylate oxygen atoms, O'_{61} and O'_{62}; not possible for pManU inthe represented conformation) and $O_5 \leftarrow H'_2$ (right to left arrow; not possible for pGulU), where the prime indicates the successor of a residue in the direction of the reducing end.

In this case, the leading intermolecular interactions responsible for chain–chain association in the junction zones are ionic interactions between the negatively-charged carboxylate groups and bridging divalent cations [2–4,29–31].

The most popular structural model for calcium-induced chain–chain association between homogulur-onate (pGulU) segments in alginates and homogalac-turonate (pGalU) segments in pectins is the so-called egg-box model [29,32]. In this model, pairs of segments in a 2_1-helical conformation are associated in a antiparallel fashion, leaving 'niches' for the calcium ions that are coordinated by (two) carboxylate and (eight) hydroxyl groups from the two chains [29,32–35].

For pGulU and pGalU, this model is compatible with the selectivity for calcium over monovalent (e.g. sodium) ions [13,29] (i.e. once bound within the gel, the Ca^{2+} ions cannot be displaced by Na^+ ions) and the stoichiometry of calcium binding [13,29,36,37] (one Ca^{2+} ion for four uronate residues), as well with the 2_1-helical conformation observed in the solid state (pGulU; acidic form [38–42], Na^+ salt [43] and, presumably, Ca^{2+} form [41]) or inferred to dominate in the gel (pGulU [29,32] and pGalU [13,33,36]). However, the egg-box model may not be the only model compatible with the available experimental data and it has been questioned in a number of recent studies, on the basis of the following arguments: (i) this model suggests a coordination number of ten for the calcium ions, while calcium-carbohydrate complexes typically rather exhibit eight-fold coordination [44]; (ii) a molecular modelling study of chain–chain association in homopolyuronates suggested two alternative models with more favorable binding energies [35]; (iii) a model of the Ca^{2+} form of pGulU in the solid state proposed on the basis of fibre diffraction data for the acidic form [38–40] suggested yet another Ca^{2+} coordination mode [42]; (iv) experi-mental evidence suggests that not only homogeneous pGulU segments, but also regular repeats of the α-[D-ManU-β(1 → 4)-L-GulU] dimer may participate in junction zones [45]; (v) small-angle X-ray scattering measurements suggest a larger width for the junction zones (compared to that expected for the egg-box dimer), even at the onset of gel formation [34,46]; (vi) X-ray scattering measurements on (slowly-formed) gels appear incompatible with junction zones exclusively associating 2_1-helices [47] (the latter study has in turn been questioned in view of the low-resolution data employed [41]). In summary, it appears that the original egg-box model [29,32] is excessively idealised in view of all recent data. In addition, although the model, initially proposed for pGulU in alginates [29,32], has often been assumed applicable to pGalU in pectins [13,33,36], the latter polyuronate presents a 3_1-helical conformation in the solid state (acidic form and Na^+ salt [48]). Although a conformational transition is indeed observed for this polymer upon dehydration [33], the question of its preferential conformation in junction zones remains

a matter of debate [10,35]. Finally, polyglucuronate (pGlcU) also forms stable gels in the presence of calcium ions [20,22]. However, the selectivity for calcium against sodium is much lower, and the mechanism involved in chain–chain association may be different.

Although a primary dimerisation mechanism is generally accepted for the cation-induced gelation of polyuronates (irrespective of the detailed structural features of chain–chain association), further (presumably weaker; see however [37]) aggregation of the dimeric junction zones may occur when Ca^{2+} is the predominant counter-ion in solution [34,37,41] (but not in the presence of a large excess of univalent cations [12,13,36]) or upon dehydration [47]. It should also be mentioned that highly-methoxylated pectins may form gels in the absence of divalent cations [11,49] (at low pH and in the presence of cosolutes like sucrose), but the mechanism of chain–chain association is different and the junction zones typically associate more than two chains.

Fibre diffraction experiments indicate a right-handed 3_1-helical conformation for pGalU (acidic form and Na^+ salt [48]) and a 2_1-helical conformation for pGulU (acidic form [38–42], Na^+ salt [43] and, presumably, Ca^{2+} form [41]), pGlcU (Ca^{2+} form [18]) and pManU (acidic form [38,39,42,43,50]) in the solid state. Calculated energy differences between the regular two- and three-fold helical conformations of homopolyuronates suggest that two types of helical conformations (the 2_1-helix and one type of three-fold helix) are almost equally stable [51], with the exception of pGulU (significantly more stable 2_1-helix). Thus, depending on the environment (e.g. solvation, packing forces, nature of the counter-ions), one or the other structure may predominate. This conformational flexibility is exploited by pManU, which adopts in the solid state a 2_1-helical conformation in its acidic form [38,39,42,43,50] but a three-fold helical conformation (presumably a left-handed 3_2-helix [51]) as a salt of monovalent cations [43]. A similar feature holds for pGalU in pectins, where a conformational transition between the gel (presumably [13,33,36] 2_1-helix) and the solid state (3_1-helix [48]) has been evidenced upon drying [36]. In contrast, pGulU maintains a 2_1-helical structure in the solid state [38–43] and presumably in the gel [41] (see however [47]). Note that this more limited flexibility of pGulU relative to pManU seems to correlate with the distribution of Gul-rich and Man-rich alginates among more rigid and more flexible tissues in plant [52].

In spite of the considerable amount of experimental data on polyuronate systems, the lack of high resolution information represents a serious obstacle in the understanding of their conformational and aggregation properties. For this reason, modelling studies represent a promising approach to shed some light on these properties [10,19,35,49,51,53–60].

A number of recent studies (in particular by Braccini et al. [35,51]) have investigated the conformational flexibility [19,51,53], energetically favored regular helical forms [19,51] and ion-binding properties [51], as well as possible chain–chain association modes [35], for the four most relevant homopolyuronates, namely poly-β(1 → 4)-D-GlcU, poly-β(1 → 4)-D-ManU, poly-α(1 → 4)-D-GalU and poly-α(1 → 4)-L-GulU (Figure 2; abreviated here as pGlcU, pManU, pGalU and pGulU, respectively). The modelling approach employed involved a combination of: (i) determination of relaxed-residue energy maps at the disaccharide level using molecular mechanics (MM3 [61–63]) energy minimisation; (ii) conformational sampling at the polymer level using a Monte Carlo procedure [53]; (iii) refinement of energetically favored regular helical models; (iv) surface probing for cation binding sites around rigid regular helices using the GRID procedure [64]; (v) rigid-body docking of pairs of helices in various relative orientations [35]. These studies suggested in particular: (i) a more important stiffness for the diaxially-linked polyuronates (pGalU, pGulU) compared to the diequatorially-linked ones (pGlcU, pManU); (ii) the existence of alternative two-fold (2_1-helix) and three-fold (3_1-helix for pGulU; 3_2-helix for pGlcU, pManU and pGulU) regular helical conformations with similar stabilities, except for pGulU (significantly higher stability for the 2_1-helix); (iii) a higher calcium binding specificity (i.e. better defined binding sites) for the two diaxially-linked polyuronates [51]; (iv) plausible chain–chain association modes (alternative to the egg-box model) for pGalU and pGulU [35]. However, three major shortcomings of this modelling strategy are that: (i) it entirely relies on an implicit description of solvation effects (continuum electrostatics); (ii) it also relies, for the first three steps, on an implicit representation of the counter-ions (i.e. their mean effects was generally approximated by considering the acidic rather than ionised form of the uronate residues); (iii) it relies, for the last two steps, on a non-dynamical (rigid) representation of the polymer chain.

Over the last few years, other types of models have been developed with the goal of providing a more mesoscopic (and thermodynamically-based) account of polyuronate–cation interactions, described as a combination of (non-specific) counter-ion condensation and (specific) tight binding effects [17,65–67]. These models go beyond a purely atomistic description of the phenomenon, and have proved quite succesful at reproducing experimental data.

A well suited theoretical method for bridging the gap between structural [35,51] (rigid and implicit solvent) and mesoscopic [17,65–67] models is explicit-solvent molecular dynamics (MD) simulation. To our knowledge, this technique has only been applied to polyuronates by four groups, to investigate calcium-bound complexes

of pGalU oligomers [56–59] (6–24 residues; 2–4 oligomers) or gellan oligomers [54] (4 residue; 2 oligomers), single-chain pGalU oligomers [68] (21 residues; charged or uncharged) or the interaction of single-chain alginates with calcium ions or calcite surfaces [60] (various Gul-Man ratios; 20 residues).

The goal of the present study is to expand the work of Braccini et al. [51] on single-chain polyuronates by taking solvent molecules, counter-ions and chain dynamics fully into account through the use of explicit-solvent MD simulation. To this purpose, we report the results of sixteen simulations (10 ns) of the same four homopolyuronates (pGlcU, pManU, pGalU and pGulU), modelled as formally infinite chains (by application of periodic boundary conditions along the chain axis with octameric or nonameric repeat units). These simulations are initiated from different starting structures, corresponding to the regular two- and three-fold helical models proposed by Braccini et al. [51] Most simulations are carried out at 300 K in the presence of calcium counter-ions (neutralising amount), but some simulations also investigate the effect of an elevated temperature or of a different counter-ion environment.

2. Computational details

2.1 Molecular dynamics simulation

All MD simulations were performed using the GROMOS96 program [69,70], together with the GROMOS 45A4 force field [71–76] (including a recently reoptimised parameter set for hexopyranose-based carbohydrates [76–78]) and the SPC water model [79]. Force-field parameters for the uronate residues were adapted from those of the corresponding hexopyranoses (substitution of the hydroxymethyl group by a carboxylate group), and are summarised in Table 1. They were validated by MD simulations of the four corresponding diuronates in water as illustrated in Figure S.1 (Suppl. Mat., available on-line).

A total of sixteen explicit-solvent simulations (10 ns) were carried out (Table 2). Eight main simulations involved the four (single-chain) homopolyuronates (pGlcU, pManU, pGalU and pGulU; Figures 1 and 2) in the presence of Ca^{2+} counter-ions at 300 K starting from two different regular helical conformations. Eight simulation variants involved a higher simulation temperature (500 K) or a different counter-ion enviroment (Na^{+} ions or Ca^{2+}-like ions with modified Lennard-Jones interaction parameters). The equations of motion were integrated using the leapfrog scheme [69,80] with a timestep of 2 fs. The SHAKE algorithm [81] was applied to constrain all bond lengths with a relative geometric tolerance of 10^{-4}. The simulations were carried out under periodic boundary conditions based on rectangular computational boxes (dimensions L_x,L_y,L_z) and in the canonical (*NVT*) ensemble. The temperature was maintained close to its reference value (300 or 500 K) by weakly coupling the solute and solvent degrees of freedom separately to a heat bath [82], with a relaxation time of 0.1 ps. Whenever required (equilibration), the

Table 1. Force-field parameters employed for the uronate residues.

Atom	Atom type	q (e)	
C_6	11	0.36	
O_{61}	2	−0.68	
O_{62}	2	−0.68	
Bond	b_0 (nm)	k_b (10^{-6}kJ·mol^{-1}·nm^{-4})	
C_5—C_6	0.153	7.15	
C_6—O_{61}	0.125	1.34	
C_6—O_{62}	0.125	1.34	
Bond-angle	θ_0 (deg)	k_θ (kJ·mol^{-1})	
C_5—C_6—O_{61}	117.0	635.00	
C_5—C_6—O_{62}	117.0	635.00	
O_{61}—C_6—O_{62}	126.0	770.00	
Improper-dihedral distortion	ξ_0 (deg)	k_ξ (kJ·mol^{-2}·deg^{-2})	
C_6—O_{61}—O_{62}—C_5	0.0	0.051	
Torsional dihedral torsion	m	cos δ	k_ϕ (kJ·mol^{-1})
O_5—C_5—C_6—O_{61}	6	+1	1.00

Note: The modifications applied to the GROMOS 45A4 force field [76] to convert a hexopyranose into the corresponding uronate are listed. The hydroxymethyl group (C_6, O_6, HO_6) is removed and replaced by a carboxylate group (C_6, O_{61}, O_{62}; the corresponding GROMOS van der Waals atom types and atomic partial charges q are indicated). The carboxylate group represents one charge group (net charge $-1e$). Following the GROMOS rules [69,70], first and second covalent neighbours are excluded from any non-bonded interaction, while third neighbour interactions are described by a special set of Lennard-Jones parameters (together with normal electrostatic interactions). The covalent interaction parameters [69,70,76] (quartic bond-stretching, cosine-harmonic bond-angle bending and harmonic improper-dihedral distortion, with corresponding reference values b_0, θ_0 and ξ_0, and force constant k_b, k_θ and k_ξ, respectively; dihedral-angle torsion, with corresponding multiplicity m, phase shift cosine $cos\ \delta$ and force constant k_ϕ) are indicated. The terms involving atoms C_4, C_5 or O_5 replace the corresponding terms in the hexopyranose. In particular, the dihedral-angle torsional terms (one or two) associated with the orientation of the hydroxymethyl group are removed and replaced by the indicated six-fold potential associated with the orientation of the carboxylate group.

Table 2. Simulated systems and simulation conditions.

Code	System	Helix	N_{res}	Ions	N_w	L_x (nm)	L_y (nm)	L_z (nm)	T_{sim} (K)
Glc2	pGlcU	2_1	8	$4Ca^{2+}$	3509	5.03	5.03	4.29	300[a]
Man2	pManU	2_1	8	$4Ca^{2+}$	3473	5.04	5.04	4.26	300[a]
Gal2	pGalU	2_1	8	$4Ca^{2+}$	2983	5.02	5.02	3.67	300[a]
Gul2	pGulU	2_1	8	$4Ca^{2+}$	2986	5.01	5.01	3.67	300[a,b]
Glc3	pGlcU	3_2	9	$5Ca^{2+} + 1Cl^-$	3777	5.06	5.06	4.58	300
Man3	pManU	3_2	9	$5Ca^{2+} + 1Cl^-$	3858	5.06	5.06	4.70	300
Gal3	pGalU	3_1	9	$5Ca^{2+} + 1Cl^-$	3475	5.06	5.06	4.20	300
Gul3	pGulU	3_2	9	$5Ca^{2+} + 1Cl^-$	3515	5.06	5.06	4.25	300
$Gul2_{Na}$	pGulU	2_1	8	$8Na^+$	2982	5.03	5.03	3.68	300[a]

Note: The simulation code, type of homopolyuronate considered (system; Figures 1 and 2), initial chain conformation (helix; 2_1-, 3_1- or 3_2- helix), number of residues in the computational box (N_{res}; imposed periodic repeat unit along a formally infinite chain), types and numbers of counter-ions (ions), number of water molecules in the computational box (N_w), box dimensions (L_x, L_y, L_z; after 0.2 ns equilibration at constant pressure) and simulation temperature (T_{sim}) are reported for the eight main simulations at 300 K performed with Ca^{2+} counter-ions and one of the eight simulation variants at 500 K or with a different counter-ion environment (Glc2H, Man2H, Gal2H, Gul2H, $Gul2_{Na}$, $Gul2_{Na}H$, $Gul2_{LJ-}$ and $Gul2_{LJ+}$; see footnotes below). Note that the L_z dimensions for the simulations at 500 K are identical to those at 300 K, because the temperature raise and the subsequent simulation were performed at constant volume. All simulations were carried out for 10 ns duration (after 0.2 ns equilibration).[a] Variants Glc2H, Man2H, Gal2H, Gul2H and $Gul2_{Na}H$ involve the same simulation conditions, but a temperature $T_{sim} = 500$ K. [b] Variants $Gul2_{LJ-}$ and $Gul2_{LJ+}$ involve the same simulation conditions, but $4Ca^{2+}$-like counterions with their effective radius (distance at the minimum of the Lennard-Jones curve for ion-water interactions) decreased ($Gul2_{LJ-}$) or increased ($Gul2_{LJ+}$) by 20%.

pressure was also maintained close to a reference value of 1 bar by weakly coupling the particle coordinates and box dimensions (isotropic coordinate scaling) to a pressure bath [82], with a relaxation time of 0.5 ps. The centre of mass motion was removed every 200 ps. Nonbonded interactions were computed using a twin-range scheme [69,83], with short- and long-range cutoff distances of 0.8 and 1.4 nm, respectively, and a frequency of 5 timesteps for the update of the short-range pairlist and intermediate-range interactions. A reaction-field correction was applied to account for the mean effect of omitted electrostatic interactions beyond the long-range cutoff distance, using a relative dielectric permittivity of 61 as appropriate for the Simple Point Charges (SPC) water model [84]. All simulations were carried out for a duration of 10 ns, and coordinates were saved to file every 1 ps for subsequent analysis.

To avoid the presence of chain-end effects and the reduction of cooperativity associated with the simulation of finite (short) oligomers [54,56–60,68], the choice was made to simulate infinite chains by taking advantage of the periodic boundary conditions (note that an alternative approach has been recently suggested [68]). To this purpose, a polymer segment consisting of N_{res} residues within the computational box (with the chain axis aligned along the z-direction) was made infinite by linking the two terminal residues via a glycosidic bond across the periodic boundary (resulting in a formally cyclic topology [85]). In this setup, the N_{res} residues are thus associated through N_{res} glycosidic linkages connecting residues i to $i + 1$ with $i = 1 \ldots N_{res} - 1$, the last linkage connecting residue N_{res} to residue 1. This approach is expected to account more appropriately for the cooperativity effects present within longer polymer chains and to entirely eliminate chain-end effects. However, one should be aware that the inclusion of an artificial periodic constraint with a repeat unit of N_{res} residues (along with a fixed end-to-end vector for this N_{res} residue repeat, as imposed by the constant-volume simulations) results in a restriction of the chain longitudinal and torsional flexibility. In particular: (i) the chain extension is artificially constrained to L_z for the repeat unit of N_{res} residues (i.e. the average raise h per residue is constrained to $N_{res}^{-1} L_z$); (ii) the formation of a regular n-fold helix is only possible when N_{res} is a multiple of n; (iii) the chain is artificially maintained close to linearity (as long as N_{res} is significantly smaller than the persistence length of the polymer, expressed on a per residue basis). Experimental estimates for the persistence lengths of the polyuronates considered (approximate, because the probed samples are seldom rigorously homopolymeric) are: 11.4 (pGlcU [20]), 4.5–9 (pManU [86–88]), 7–5 (pGalU [89,90]) and 5–17 nm (pGulU [91,92]), while corresponding theoretical estimates for the acidic forms [51] are 10.5, 11.9, 16.6 and 21.0 nm. Considering a distance of 0.56 and 0.48 nm between glycosidic oxygen atoms for ideal chair conformations involved in diequatorial and diaxial linkages, respectively, the latter values correspond to about 20 (pGlcU, pManU) or 40 (pGalU, pGulU) residues.

For each of the four polymers considered, two alternative types of regular helices were selected as starting conformations for the simulations [51]: 2_1- and (left-handed) 3_2 -helix for pGlcU, pManU and pGulU, or 2_1- and (right-handed) 3_1-helix for pGalU. The 2_1-helices were investigated for systems with an octameric ($N_{res} = 8$) repeat unit, and the 3_1- and 3_2-helices for systems with a nonameric ($N_{res} = 9$) repeat unit. Initial coordinates for these eight chain configurations were generated using the program InsightII [93], assuming ideal $^4C_1$ (pGlcU, pManU, pGalU) or $^1C_4$ (pGulU) ring geometries and using the reference ϕ and ψ glycosidic

Table 3. Glycosidic linkage conformation and carboxylate group orientation.

Code	ϕ (deg)	ϕ_{ref} (deg)	ψ (deg)	ψ_{ref} (deg)	γ (deg)	γ_{ref} (deg)	τ_γ (ns)
Glc2	252.6 (24.1)	268.7	109.3 (13.8)	84.7	115.9 (21.6)	129	>4
Man2	260.2 (35.2)	274.5	105.7 (16.0)	83.6	108.4 (17.5)	126	>6
Gal2	103.0 (16.2)	94.5	254.5 (16.5)	267.9	142.4 (30.2)	136	0.16
Gul2	261.4 (15.1)	275.8	98.3 (16.1)	84.7	218.0 (31.2)	225	0.25
Glc3	269.3 (17.3)	293.0	129.7 (15.3)	132.8	111.6 (17.4)	134	>8
Man3	279.6 (17.9)	295.8	108.1 (12.9)	135.4	109.4 (17.0)	127	>9
Gal3	73.7 (14.3)	74.6	215.6 (18.3)	214.8	151.7 (21.4)	154	0.74
Gul3	289.8 (14.1)	295.9	137.5 (19.2)	135.6	211.1 (21.5)	217	0.55
$Gul2_{Na}$	261.6 (15.3)	275.8	98.1 (16.4)	84.7	211.1 (21.5)	217	0.16
$Gul2_{LJ-}$	261.6 (15.2)	275.8	98.1 (16.7)	84.7	211.1 (21.5)	217	0.14
$Gul2_{LJ+}$	261.6 (15.1)	275.8	98.1 (15.9)	84.7	211.1 (21.5)	217	0.14
Glc2H	251.2 (26.4)	268.7	110.6 (17.6)	84.7	115.9 (21.6)	129	0.25
Man2H	251.7 (39.2)	274.5	113.6 (22.1)	83.6	108.4 (17.5)	126	0.34
Gal2H	102.3 (19.5)	94.5	255.0 (19.2)	267.9	142.4 (30.2)	136	0.05
Gul2H	260.2 (19.9)	275.8	99.4 (19.4)	84.7	211.1 (21.5)	217	0.05
$Gul2_{Na}H$	260.2 (19.7)	275.8	99.4 (19.2)	84.7	211.1 (21.5)	217	0.05

Note: Mean values and standard deviations (along the time series; between parentheses) of the glycosidic dihedral angles ϕ and ψ, and of the dihedral angle γ characterising the orientation of the carboxylate group, averaged over the N_{res} linkages for the different simulations (Table 2). The γ values were refolded to a single period of 180° prior to averaging (these periods were 30–210° for pGlcU and pManU, 60–240° for pGalU and 120–300° for pGulU; Figure 3). The values ϕ_{ref}, ψ_{ref} and γ_{ref} correspond to the dihedral-angle values reported for the different helix types by Braccini et al. [51], based on MM3 relaxed-residue energy maps for the corresponding diuronic acids (ψ_{ref} was converted from the $\tilde{\psi}$ to the ψ definition). The timescale τ_γ associated with the rotational isomerisation of the carboxylate groups is also reported. See Section 2.2 for the definitions of ϕ, ψ, $\tilde{\psi}$ and γ. Averaging was performed over the final 9 ns of the simulations.

dihedral angle values (ϕ_{ref} and ψ_{ref}; Table 3) reported for the different helix types by Braccini et al. [51] (based on MM3 relaxed-residues energy maps for the corresponding diuronic acids). The initial box dimension L_z was set to N_{res} h_{ref}, where h_{ref} is the raise per residue associated with the selected ϕ_{ref} and ψ_{ref} values in the specific chain (Table 4). The two other box dimensions L_y and L_z were set to 5 nm. The computational boxes were brought to overall neutrality by inclusion of counter-ions (4 Ca^{2+} or 8 Na^+ for $N_{res} = 8$; 5 Ca^{2+} + 1 Cl^- for $N_{res} = 9$), and filled to a water density of about 1 g cm^{-3}. After energy minimisation, equilibration was carried out by performing 0.2 ns MD simulation at constant pressure (1 bar; allowing for a small variation of L_z from its initial value

Table 4. Helical parameters.

Code	h (nm)	h_{ref} (nm)	h_{exp} (nm)	M	θ (deg)
Glc2	0.537 (0.008)	0.516	0.516[a]	4	180.0 (29.8)
Man2	0.532 (0.008)	0.514	0.518[b]	4	180.0 (39.6)
Gal2	0.459 (0.011)	0.425	–	4	180.0 (23.1)
Gul2	0.459 (0.012)	0.427	0.436[c]	4	180.0 (20.9)
Glc3	0.509 (0.013)	0.506	–	6 (99.4), 5	239.7 (20.3)
Man3	0.523 (0.008)	0.506	–	5 (99.7), 6[d]	200.1 (22.1)
Gal3	0.467 (0.011)	0.443	0.447[e]	3	120.0 (24.4)
Gul3	0.473 (0.010)	0.442	–	6	240.0 (24.4)
$Gul2_{Na}$	0.459 (0.012)	0.427	–	4	180.0 (21.4)
$Gul2_{LJ-}$	0.459 (0.012)	0.427	–	4	180.0 (21.5)
$Gul2_{LJ+}$	0.459 (0.011)	0.427	–	4	180.0 (20.8)
Glc2H	0.537 (0.010)	0.516	–	4	180.0 (34.1)
Man2H	0.532 (0.009)	0.514	–	4 (99.9), 3	179.9 (48.3)
Gal2H	0.459 (0.013)	0.425	–	4 (99.9), 3	179.9 (27.5)
Gul2H	0.459 (0.012)	0.427	–	4	180.0 (27.0)
$Gul2_{Na}H$	0.459 (0.014)	0.427	–	4	180.0 (26.9)

Note: Mean values and standard deviations (along the time series; between parentheses) of the turn angle θ and helix raise h, averaged over the N_{res} linkages, together with the number M of full right-handed turns per N_{res} residues, for the different simulations (Table 2). The values h_{ref} correspond to the regular model helices proposed by Braccini et al. [51] based on MM3 relaxed-residue energy maps for the corresponding diuronic acids, and the values h_{exp} to experimental (fibre diffraction; solid state) data (see footnotes below). For the M entries, the possible occurence of two distinct values along a given simulation is indicated, together with the corresponding occurence for the major component (between parentheses; in percent). See Section 2.2 for the definitions of θ, h and M. Averaging was performed over the final 9 ns of the simulations.[a] Heyraud et al. [18]. [b] Atkins et al. [38,39,50]. [c] Atkins et al. [38–40] and Sikorski et al. [41] (Li et al. [47] report a lower value of 0.39 nm, which they attribute to a 3_1-helical conformation). [d] The corresponding distribution of M for Man3 when calculated over the entire (10 ns) trajectory is 5 (89.7%) and 6 (10.3%). [e] Walkinshaw et al. [48].

N_{res} h_{ref}), increasing the temperature from 50 to 300 K in six succesive steps, and the resulting configurations used for the production simulations (constant volume; fixed L_z).

The eight main simulations were carried out in the presence of Ca^{2+} counter-ions (and one Cl^- for $N_{res} = 9$) at a temperature of 300 K (constant volume). In adition, eight simulation variants were carried out for a subset of systems with either or both of the following modifications: (i) an artificially elevated temperature of 500 K; (ii) the inclusion of Na^+ counter-ions (instead of Ca^{2+}) or of Ca^{2+}-like counter-ions with their effective radius (distance R^*_{min} at the minimum of the Lennard-Jones curve for ion-water interactions) decreased or increased by 20% relative to $R^*_{min} = 0.335$ nm (for the GROMOS Ca^{2+} ion in SPC water). A summary of the simulated systems and simulation conditions is provided in Table 2.

2.2 *Analysis of the trajectories*

The analysis of the trajectories was performed in terms pyranose ring conformation, carboxylate group orientation, glycosidic dihedral-angle conformation, helical parameters, intramolecular hydrogen bonding, ion distribution and binding, chain translational and rotational diffusion, and ionic diffusion. All dihedral-angle values were defined using the IUPAC sign convention [94], the corresponding numerical values were selected within the range [0; 360°], and the corresponding distributions were computed with a bin width of 1°.

The ring conformation was assesed for all N_{res} residues by monitoring the dihedral angles α_k, $k = 1 \ldots 6$ (C_1—C_2—C_3—C_4, C_2—C_3-C_4—C_5, C_3—C_4—C_5—O_5, C_4—C_5-O_5—C_1, C_5—O_5—C_1—C_2 and O_5—C_1—C_2—C_3). The resulting ring shape (chair, boat or other) was defined by assigning the successive dihedral angles to wells of width 60° centred at the six values corresponding to eclipsed or staggered rotamers. The orientation of the corresponding carboxylate group was assessed by monitoring the dihedral angles γ_1 (O_5-C_5-C_6-O_{61}) and γ_2 (O_5-C_5-C_6-O_{62}). Due to symmetry, these two dihedral angles are expected to present identical properties (given sufficient sampling) and are collectively referred to as γ.

The glycosidic dihedral angles ϕ and ψ associated with the N_{res} glycosidic linkages were defined (according to IUPAC recommendations [94]) as O_5-C_1-O_1-C'_4 and C_1-O_1-C'_4-C'_3, respectively. An alternative definition $\tilde{\psi}$ is sometimes used for the latter angle [51] as C_1-O_1-C'_4-C'_5. The two definitions are related by the approximate relationships $\tilde{\psi} = \psi + 120°$ (S-stereochemistry at C'_4; D-GlcU, D-ManU, L-GulU) or $\tilde{\psi} = \psi - 120°$ (R-stereochemistry at C'_4; D-GalU). The corresponding local helical parameters were defined in the following way [95]. The helix raise h was measured by the distance between the 'reference points' of two successive residues, this point being defined here as the centre of geometry of the ring atoms C_2, C_3, C_5 and O_5. The helix turn angle θ was measured by the dihedral angle between the 'reference vectors' of two successive residues, this vector being defined here as the projection of the vector connecting the midpoint of the C_2—C_3 bond to the midpoint of the C_5—O_5 bond onto the xy-plane (perpendicular to the helix axis). Values of θ within ranges of ± 30° around 120, 180 or 240° were associated to local 3_1-, 2_1- or 3_2-helical conformations, respectively. Due to the (artificial) periodicity constraint along the z-axis of the computational box, the sum of θ values is always an integer multiple of 360°. However, the associated integer multiplicative factor M, representing the number of full right-handed turns per N_{res} residues, may vary in time in the range $0 \cdot N_{res} - 1$. This parameter was also monitored along the different simulations. A regular n_m helix compatible with the periodic repeat unit of N_{res} residues artificially imposed in the present simulations (i.e. for which n is a divisor of N_{res}) will be characterised by $M = n^{-1} \cdot N_{res} \cdot m$. For example, a regular 2_1-helix with $N_{res} = 8$ will be associated with $M = 4$. Similarly, regular 3_1- and 3_2-helices with $N_{res} = 9$ will be associated with $M = 3$ and $M = 6$, respectively. It is important to realise that although M values can be associated to both simulated configurations and regular helices, it would be incorrect to assume that a simulated configuration with a given M value is necessarily a regular helix of the corresponding type.

Intramolecular hydrogen bonding was analysed considering all hydroxyl groups as potential hydrogen-bond donors, and all hydroxyl, ring or carboxylate oxygen atoms as potential acceptors. The presence of a hydrogen bond was defined by a maximal hydrogen–oxygen distance of 0.25 nm and a minimal oxygen–hydrogen–oxygen angle of 135°. A hydrogen bond between a hydroxyl and a carboxylate group was assumed to be present if the hydroxyl group formed a hydrogen bond with either (or both) of the carboxylate oxygen atoms.

The distribution of the N_{ion} positive (Ca^{2+} or Na^+) counter-ions along the chain was visualised by superimposing successive trajectory frames (chain and counter-ions) onto the initial (equilibrated) chain configuration (rotational and translational fit based on the C_2, C_3, C_5 and O_5 atoms), and displaying the positions of all positive ions at 10 ps intervals (excluding the first 1 ns of simulation; these figures are complemented by two-dimensional radial distribution functions $g_{2D}(r)$ for the ionic coordinates in the xy-plane relative to the chain axis). The counter-ion distribution was further analysed in terms of the radial distribution function $g(\rho)$ corresponding to the smallest (minimum-image) distance

ρ between any of the two carboxylate oxygen atoms and the closest counter-ion (excluding the first 1 ns of simulation). This function is defined in such a way that the integral of $4\pi\rho^2 g(\rho)$ over the entire simulation box (or any larger volume) is equal to $V = L_x\ L_y\ L_z$. In addition, ion-binding events were monitored for the N_{res} residues, by assigning two cutoff values ρ_t and ρ_l (with $\rho_t < \rho_l$) to the distance ρ. The condition $\rho \leq \rho_t$ was associated to a tight binding event (TB; contact ion pair), the condition $\rho_t < \rho \leq \rho_l$ to a loose binding event (LB; solvent-separated ion pair), while $\rho > \rho_l$ corresponded to the absence of ion binding. The values of ρ_t and ρ_l were chosen as the locations of the first and the second minima in $g(\rho)$ for a given type of ion, i.e. ρ_t was set to 0.33 (Ca^{2+}), 0.30 (Na^{+}), 0.31 (Ca^{2+}-like ion with R^{*}_{min} decreased by 20%) or 0.35 nm (Ca^{2+}-like ion with R^{*}_{min} increased by 20%), while the corresponding values of ρ_l were set to 0.57, 0.54, 0.52 or 0.59 nm. The binding (LB or TB) of the carboxylate group of a given residue to a counter-ion that is simulateneously bound (LB or TB) to the carboxylate group of a different residue was referred to as a double binding (DB; ion bridging) event. Two different types of DB events were further distinguished depending on whether they involved the carboxylate groups of two neighbour residues (DB_n) or of two second-neighbour residues (DB_s; i.e. separated by single residue along the chain). The coordination of counter-ions with the other sugar oxygen atoms (O_1, O_2, O_3 or O_5) was also monitored in an analogous way (radial distribution functions and binding events, using $\rho_t = 0.34$ and $\rho_l = 0.56$ nm). All radial distribution functions were computed with a bin width of 0.01 nm.

Diffusion coefficients were calculated by monitoring the mean-square displacements $Q_q(t)$ of various time dependent quantities q(t), with averaging over all possible time origins (excluding the first 1 ns of simulation). The corresponding diffusion coefficients D_q were calculated based on the Einstein relation, taking into account the dimension n (1, 2 or 3) of the quantity q. In practice, D_q was estimated from the slope of a regression line fitting $Q_q(t)$ over the interval from 0 to 3 ns where these functions were found to be approximately linear. The quantities q considered and the corresponding diffusion coefficients D_q were: (i) the z-coordinate of the chain centre (centre of geometry of the 'reference points' of all residues; with $n = 1$), to evaluate the chain longitudinal diffusion constant D_z; (ii) the coordinate vector of the chain centre in the xy-plane (with $n = 2$), to evaluate the chain transverse diffusion constant D_{xy}; (iii) the chain orientation angle Θ (mean of the 'reference angles' of all residues; with $n = 1$), to evaluate the chain rotational diffusion constant D_Θ; (iv) the z-coordinate of a given counter-ion (with $n = 1$), to evaluate longitudinal diffusion constants $D_{i,z}$ for all (positive) counter-ions $i = 1 \ldots N_{\text{ion}}$; (v) the coordinate vector of a given counter-ion in the xy-plane (with $n = 2$), to evaluate the transverse diffusion constants $D_{i,xy}$ for all (positive) counter-ions $i = 1 \ldots N_{\text{ion}}$. While evaluating the corresponding time series q(t), care was taken to follow periodic coordinates as they diffused across different periods, without 'refolding' to the reference interval.

Life-times of specific properties (dihedral angle in a specific well, local helical conformation of a given type, formation of inter-residue hydrogen bonds and ion binding events) were estimated by averaging the durations of all uninterrupted occurences of the specific property over the trajectories. However, to avoid an excessive influence of occurences or interruptions with very short durations on the overall statistics, an allowed excursion time τ_{exc} (set to 10 ps) was applied, i.e. occurences or interruptions were only accepted as such when their durations exceeded τ_{exc}.

3. Results and discussion

3.1 Ring conformation and carboxylate group orientation

The mean values and standard deviations of the ring dihedral angles α_k, $k = 1 \ldots 6$, averaged over the N_{res} residues, are reported in Table S.1 (Suppl. Mat.) for all simulations. The reported values are all consistent with leading $^4C_1$ (pGlcU, pManU, pGalU) or $^1C_4$ (pGulU) chair conformations (Figure 1), with deviations from the ideal values (60 or 300°) no larger that 10°. The leading chair conformation accounts for 99.7–100.0% of the sampled configurations at 300 K, or 98.1–99.8% at 500 K. The remaining conformations are slightly distorted chair forms, with very short lifetimes (typically ≤ 1 ps). Note that glucuronate appears to be slightly more flexible compared to the other uronates. A similar observation was reported previously [78] in the context of hexopyranoses.

The probability distributions of the dihedral angle γ characterising the orientation of the carboxylate group, averaged over the N_{res} residues, are displayed in Figure 3 for the eight main simulations (300 K, Ca^{2+} counter-ions; Table 2). The corresponding probability distributions for the eight simulation variants (500 K or different counter-ion environment), provided in Figure S.2 (Suppl. Mat.), are qualitatively similar to the former ones. The mean values and standard deviations associated with these distributions are reported in Table 3 for all simulations, together with the corresponding timescales τ_γ for rotational isomerisation between the two main (equivalent) carboxylate group orientations, and the values γ_{ref} suggested for the different types of regular helices by Braccini et al. [51]

As expected, the γ distributions are essentially periodic of period 180°, the conformations corresponding γ and $\gamma + 180°$ representing equivalent carboxylate

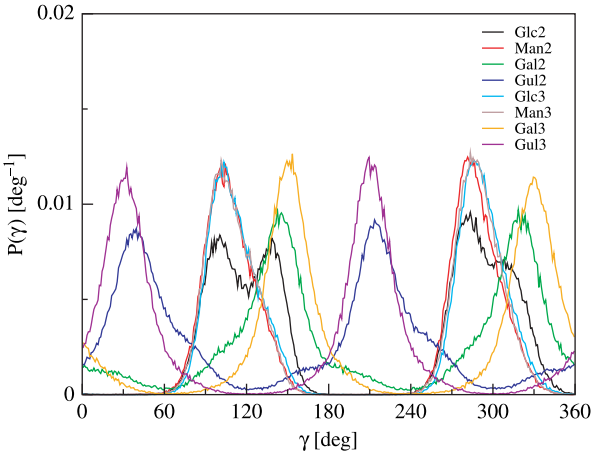

Figure 3. Normalised probability distributions of the γ dihedral angle characterising the orientation of the carboxylate group, averaged over the N_{res} residues, for the eight main simulations (300K, Ca^{2+} counter-ions; Table 2). The γ distribution accounts for the combined distributions of the two symmetry-related dihedral angles γ_1 and γ_2. See Section 2.2 for the definitions of γ_1, γ_2 and γ. Averaging was performed over the final 9 ns of the simulations.

group orientations. Minor deviations from this expected periodicity, especially visible for simulation Glc2, only arise from incomplete sampling. Over a single 180° period, all distributions are essentially unimodal except for simulation Glc2. Focusing on the eight main simulations, the corresponding average values (Table 3) are found to be about 115° (pGlcU, pManU), 145° (pGalU) and 215° (pGulU). These values are in good agreement with the corresponding reference values γ_{ref}, with deviations of at most 25°. A possible explanation for the dominance of these specific rotamers is that they involve approximately equal distances between the two carboxylate oxygen atoms and the glycosidic oxygen, thereby minimising the corresponding Coulombic repulsion. However, other electronic effects, solvation, inter-residue hydrogen bonding and cation binding may *a priori* also influence these conformational preferences. For simulation Glc2, a second peak in the γ distribution is seen at about 130–140° (Figure 3), which is not present in simulation Glc3. Besides this change, the distributions are only sensitive to the initial helical conformation for pGalU and pGulU, where the distribution becomes narrower and the peak position is shifted by about +10° or −10°, respectively, when changing from the two- to the three-fold helix.

At 300 K, the timescales τ_γ associated with the rotation of the carboxylate group are significantly longer for pGlcU and pManU (>4 ns) compared to pGalU and pGulU (160–740 ps). Expectedly, rotational isomerisation is much faster at 500 K (in particular for pGlcU and pManU). For pGulU at 300 K, a change in the counter-ion environment has essentially no influence on τ_γ.

The origin of the above differences between diequatorially- and diaxially-linked homopolyuronates in terms of the dependence of the γ distribution and of the τ_γ value on the helix type at 300 K remains unclear. In particular, these differences can not be easily rationalised on the basis of the hydrogen bonds involving the carboxylate groups (Section 3.4) or of counter-ion binding or bridging (Section 3.5).

3.2 *Glycosidic linkage conformation*

The probability distributions of the glycosidic dihedral angles ϕ and ψ, averaged over the N_{res} linkages, are displayed in Figure 4 for the eight main simulations. The corresponding probability distributions for the eight simulation variants, provided in Figure S.3 (Suppl. Mat.), are qualitatively similar to the former ones. The mean values and standard deviations associated with these distributions are reported in Table 3 for all simulations, and compared with the values ϕ_{ref} and ψ_{ref} suggested for the different types of regular helices by Braccini et al. [51]. A representation of the trajectories in the form of configurations sampled on the Ramachandran (ϕ, ψ) map is also provided in Figures S.4 and S.5 (Suppl. Mat.) for all simulations.

The conformational preferences around the glycosidic dihedral angle ϕ are expected to be dominated by the *exo*-anomeric effect [97–101] which stabilises (assuming the chair conformations of Figure 1) conformers with ϕ values of about 300° (D-enantiomer, β-linkage; pGlcU, pManU), 60° (D-enantiomer, α-linkage; pGalU) and 300°(L-enantiomer, α-linkage; pGulU). These preferences are essentially respected in the reference values ϕ_{ref} suggested by Braccini et al. [51]. These values are comprised between 268.7 and 295.9° for pGlcU, pManU and pGulU, while they are 74.6 or 94.5° for pGalU. The associated ψ_{ref} values are not influenced by such a large stereoelectronic effect, and probably correspond to conformations affording a good compromise between steric effects, inter-residue hydrogen bonding and solvation given the above ϕ_{ref} preferences.

Focusing on the eight main simulations, the average ϕ and ψ values agree reasonably well with the corresponding ϕ_{ref} and ψ_{ref} values for the same helix type. However, the deviations of the simulation averages from the reference values (ranging between −16.2 and +8.5° for ϕ or between −27.3 and +24.6° for ψ), as well as the fluctuations observed during the simulations (ranging between 14.1 and 35.2° for ϕ or between 12.9 and 19.2° for ψ), remain significant. The largest deviations relative to the reference values are found for simulations Glc2, Man2 and Man3. Note, however, that perfect agreement should probably not be expected because: (i) the reference values are associated with rigid (idealised) configurations, while the present averages characterise conformational

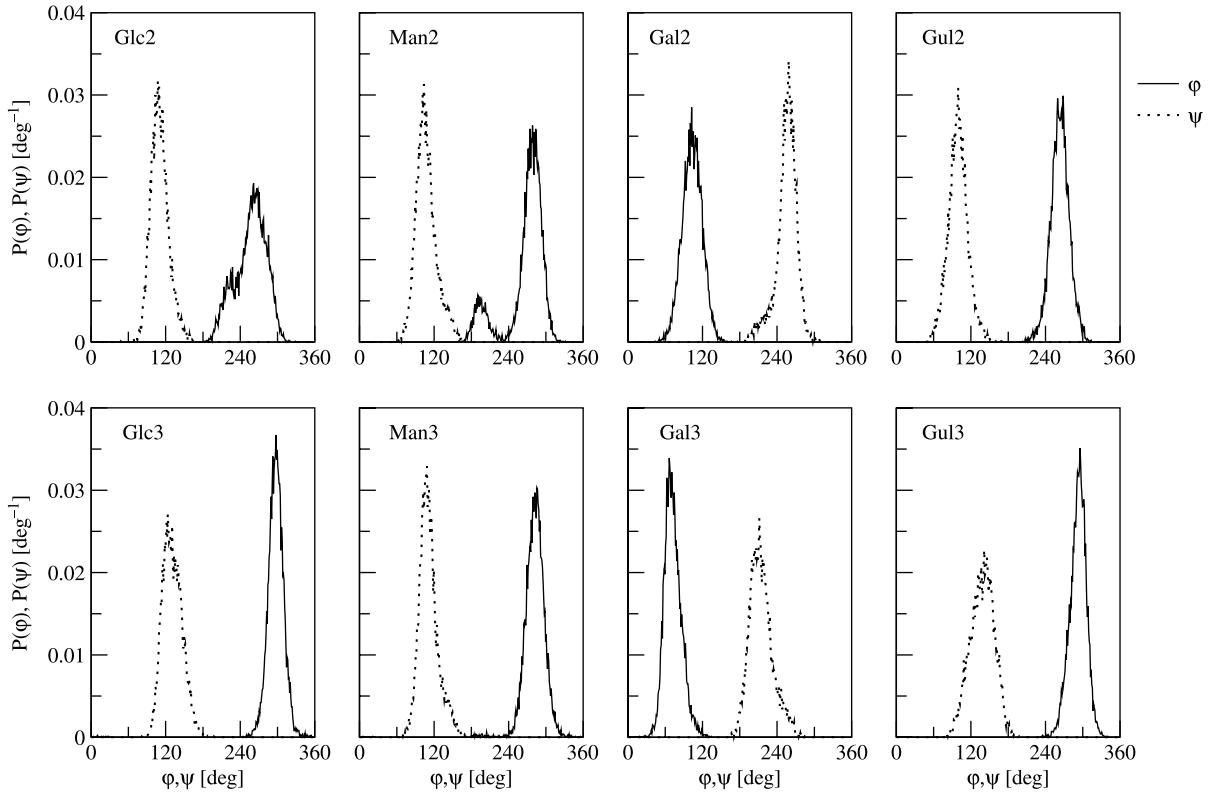

Figure 4. Normalised probability distributions of the glycosidic dihedral angles ϕ and ψ, averaged over the N_{res} linkages, for the eight main simulations (300 K, Ca^{2+} counter-ions; Table 2). See Section 2.2 for the definitions of ϕ and ψ. Averaging was performed over the final 9 ns of the simulations.

ensembles at 300 K; (ii) the reference values are based on relaxed-residue energy maps for uronic acids (protonated form) at the disaccharide level, while the present averages are representative for formally infinite polyuronate chains (deprotonated form); (iii) the reference values are based on implicit-solvent calculations with the MM3 force field [61–63] in the absence of counter-ions, while the present averages are based on explicit-solvent MD simulations with the GROMOS force field [69,70,76] including counter-ions; (iv) the reference values were explicitly adjusted to be compatible with the formation of regular two- or three-fold helices, while no such constraint is applied in the present simulations. Nevertheless, as can be seen from Figure S.4 (Suppl. Mat.), the reference conformation of Braccini et al. is always included (and usually centred; except for Glc2 and Man2) in the area of the Ramachandran map visited by the simulations.

The probability distributions of the ϕ and ψ dihedral angles in the eight main simulations (Figure 4) are all essentially unimodal, with the exception of the ϕ distributions for simulations Glc2 and Man2. This feature explains the particularly high fluctuations of ϕ (24.1 and 32.2°, respectively), and possibly also the more important deviations from ϕ_{ref} (-16.1 and -14.3°, respectively), observed in these two simulations (Table 3). The corresponding ϕ distributions can be deconvoluted as the sum of two quasi-Gaussian peaks, centred at 219 and 261° (relative populations 18 and 82%, respectively) for Glc2, or at 195 and 279° (relative populations 21 and 79%) for Man2. The corresponding ψ values (evaluated separately for the subset of conformers with $\phi < 233$° and $\phi > 233$°) are 100.0 and 112.1° for Glc2, or 97.1 and 108.1° for Man2. In both systems, the second (major) peak is in the expected range for a local 2_1-helical conformation. However, the first (minor) peak is not in the appropriate range for a local 3_2-helical conformation. As will be seen below (Section 3.3), it corresponds to a local 3_1-helical conformation. The simulations initiated from the corresponding three-fold helices (Glc3 and Man3) are characterised by an essentially unimodal probability distribution for ϕ, although the minor conformer can also be detected in simulation Man3 (with a marginal occurrence). Note that these minor conformers are the only ones sampled in the present simulations (with a non-negligible population) that are not in the expected range for stabilisation by the *exo*-anomeric effect.

The time series of the ϕ and ψ dihedral angles for the individual N_{res} linkages are displayed in Figures 5 and 6

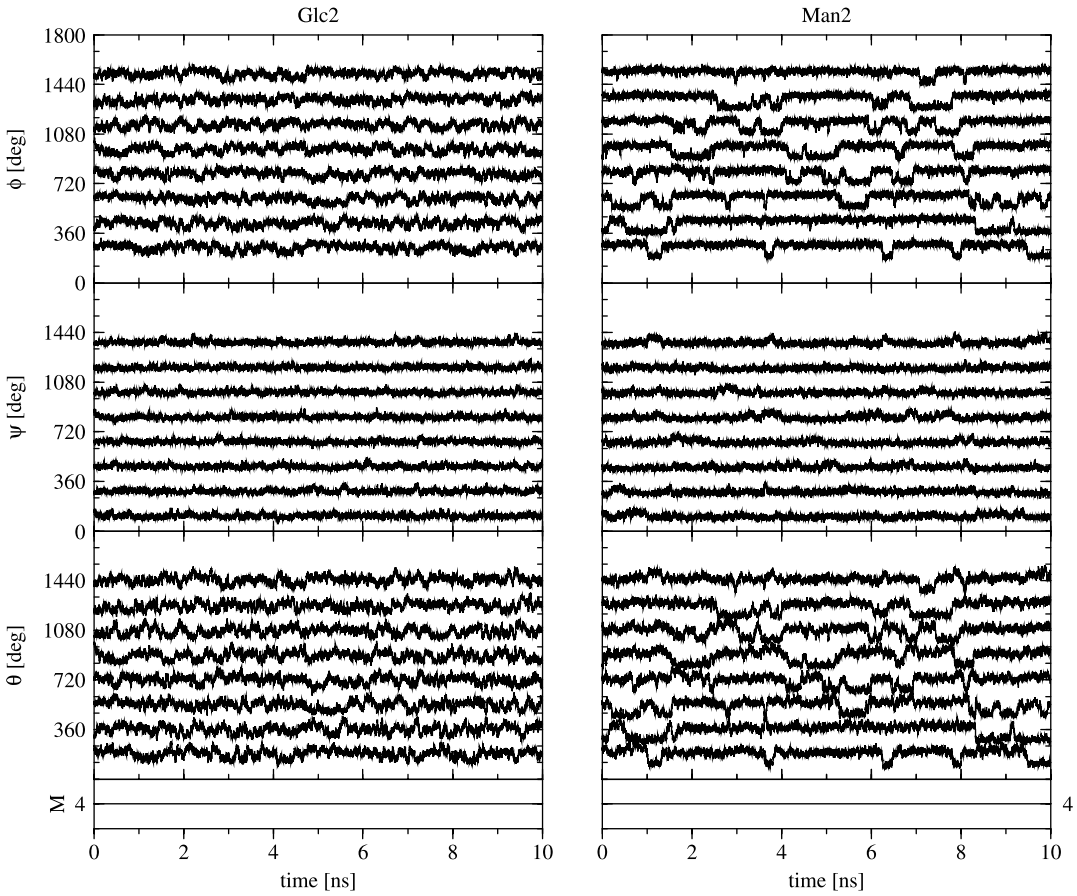

Figure 5. Time series of the glycosidic dihedral angle ϕ and ψ, and of the turn angle θ, for the N_{res} linkages, together with that of the number M of full right-handed turns per N_{res} residues,as monitored during simulations Glc2 and Man2 (Table 2). See Section 2.2 for the definitions of ϕ, ψ, θ and M. Successive curves (ϕ, ψ and θ) corresponding to the different residues along the chain are shifted upwards by 180° for readability.

for simulations Glc2, Man2, Glc3 and Man3. Hopping between the minor and major conformers is evident in the time series of the ϕ dihedral angle for the individual linkages during simulations Glc2 and Man2 (Figure 5) and, to some extent, Man3 (Figure 6). The transitions are local and asynchronous along the chain, i.e. only a few linkages adopt the minor conformation simultaneously. The average residence time of a dihedral angle in the latter conformation ($\phi < 233°$) is 70 ps for Glc2 and 220 ps for Man2. For simulations Glc3 and Man3, very brief excursions can be observed (of a few ps duration) toward ϕ values comprised between 0 and 120° (Figure 6). Note, finally, that none of the transitions described above for ϕ are associated with significant changes in ψ.

The average ϕ and ψ values at 500 K do not differ significantly from those at 300 K, while the corresponding fluctuations are somewhat enhanced (Table 3). For pGulU at 300 K, the nature of the counter-ions has essentially no influence on the corresponding average values and fluctuations.

3.3 Helical parameters

The probability distributions of the helix raise h and turn angle θ, averaged over the N_{res} linkages, are displayed in Figure 7 for the eight main simulations, and in Figure S.6 (Suppl. Mat.) for the eight simulation variants. The latter distributions are qualitatively similar to the former ones. The mean values and standard deviations associated with these distributions are reported in Table 4 for all simulations, together with the corresponding values h_{ref} for the regular helical models proposed by Braccini et al. [51] and with experimental values h_{exp} from fibre diffraction measurements in the solid state [18,38–41,47,48].

Due to the (artificial) periodicity constraint imposed to the chains along the z-axis of the computational box (and the fact that L_z is fixed in the present constant-volume simulations), the instanteneous value of h averaged over all linkages along the chains (and thus, obviously, its time-average) is always equal to $N_{res}^{-1} L_z$ (compare Tables 2 and 4). Focusing on the eight main

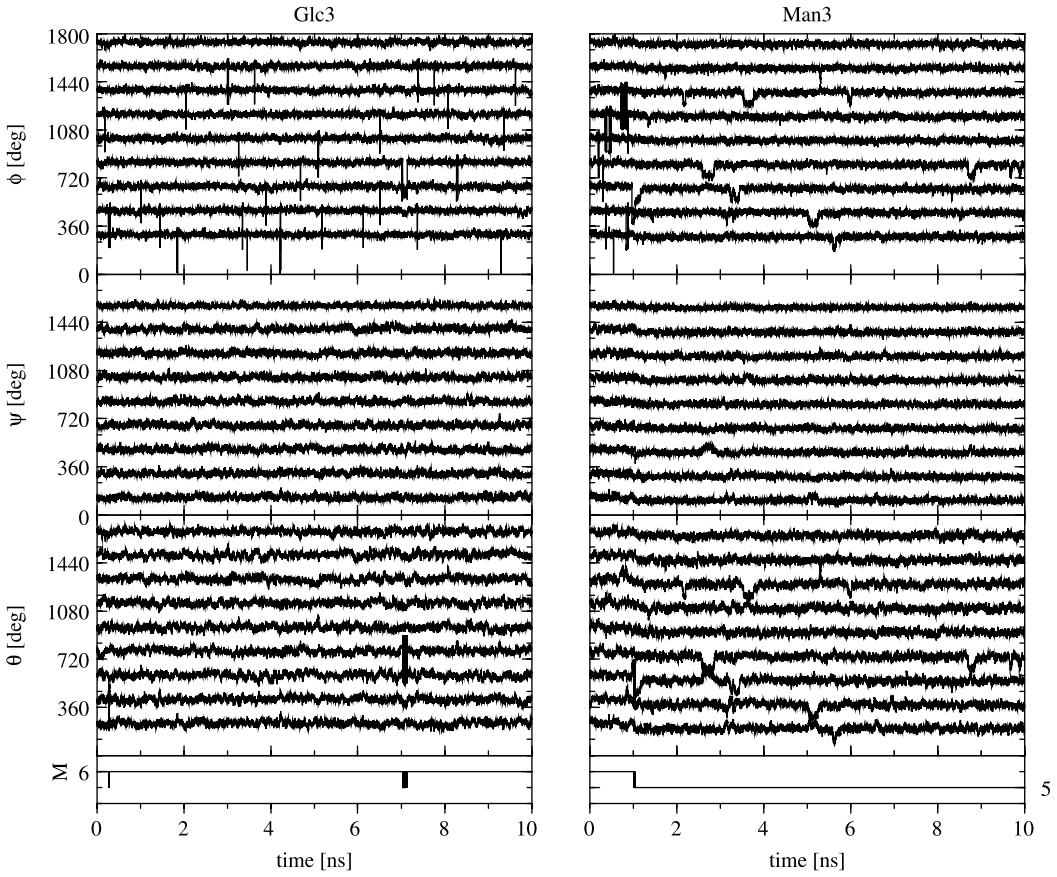

Figure 6. Time series of the glycosidic dihedral angle ϕ and ψ, and of the turn angle θ, for the N_{res} linkages, together with that of the number M of full right-handed turns per N_{res} residues, as monitored during simulations Glc3 and Man3 (Table 2). See Section 2.2 for the definitions of ϕ, ψ, θ and M. Successive curves (ϕ, ψ and θ) corresponding to the different residues along the chain are shifted upwards by 180° for readability.

simulations, diequatorialy-linked chains (pGlcU, pManU) are more extended than diaxialy-linked ones (pGalU, pGulU), by about 16–17% and 8–12% for the simulations initiated from two- and three-fold, helices respectively. This difference is expected since a rigid chair conformation places diequatorial O_4 and O_1 atoms at a distance of about 0.56 nm, compared to only about 0.48 nm for the corresponding diaxial configuration. For the diequatorially-linked chains, h is higher by about 2–6% for the simulations initiated from a two-fold helix compared to those initiated from the three-fold helix. For the diaxially-linked chains, the opposite is true and the values are higher by about 2–3% for the three-fold relative to the two-fold helices. The distributions of h values are all unimodal (Figure 7).

The average values of h are somewhat higher (by 0.5–7%) compared the h_{ref} values for the corresponding model regular helices, themselves being very close to the experimental values h_{ref} in the solid state (Table 4). This results from a slight expansion of the chains during the 0.2 ns equilibration period at constant pressure (Section 2.1). Such a difference probably results from the introduction of thermally-induced conformational disorder (deviation from rigid regular helices in the simulated ensemble at 300 K; $h \neq h_{ref}$) and of solvation forces (replacing the packing forces present in the solid sate; $h \neq h_{exp}$).

Assuming fixed bond lengths and angles as well as rigid pyranose ring conformations, the helix turn angle θ defining the local helicity is a unique function of the glycosidic dihedral angles ϕ and ψ. A representation of the trajectories correlating the (ϕ, θ) and (ψ, θ) dihedral angle pairs is provided in Figures S.7-S.10 (Suppl. Mat.) for all simulations. These maps indicate that θ is about equally sensitive to variations in both ϕ and ψ. The (ϕ, θ) maps corresponding to simulations Glc2 and Man2 also show that the minor conformers observed in the corresponding ϕ distributions (Section 3.2) can be associated to local 3_1-helical conformations. The average θ values for these minor conformers ($\phi < 233°$) are 140.5 and 115.7° for Glc2 and Man2, respectively (local 3_1-helical conformation), to be compared with 191.8 and 197.7° for the major conformers (local 2_1-helical conformation).

Due to the (artificial) periodicity constraint imposed to the chains in the present simulations, the instantaneous value of θ, averaged over all linkages along the chain, is always an integer multiple of N_{res}^{-1} 360°. However, because the corresponding integer multiplicative factor M (number of full right-handed turns for the repeat unit of N_{res} residues) may vary in time, the same property need not be satisfied by the corresponding time average (Table 4). In practice, however, the value of M remains identical or nearly identical (Glc3, Man2H, Gal2H) to the corresponding value for the initial model helix throughout all but one simulations (Man3), i.e. M is 4 for the simulations initiated from 2_1-helices ($N_{res} = 8$), 3 for those initiated from 3_1-helices ($N_{res} = 9$) and 6 for those initiated from 3_2-helices ($N_{res} = 9$). Simulation Man3 represents the exception with a dominant M value of 5 (over the final 9 ns of the simulation) and an average θ value close to 200°.

The time series of θ for the individual N_{res} linkages, together with the corresponding time series of M, are displayed in Figures 5 and 6 for simulations Glc2, Man2, Glc3 and Man3. The transitions observed in ϕ between major and minor conformers for simulations Glc2, Man2 and, to some extent, Man3 (Section 3.2) clearly correspond to simultaneous transitions in θ. The M value is always 4 in simulations Glc2 and Man2. It is nearly always 6 in simulation Glc3 (besides two short transitions to a value of 5). The situation is different for simulation Man3. During the first 1.02 ns of this simulation, the M value is 3 (as appropriate for a 3_2-helix with $N_{res} = 9$, i.e. for the starting structure). However, at this time point, the value abruptly changes to 5 (as appropriate for a 9_5-helix) and remains constant for the rest of the simulation.

The occurences of regular or quasi-regular helices are reported in Table 5 for all simulations (final 9 ns), together with the five most frequently encountered distributions of linkages among different local helical conformations. Although the value of M essentially stays identical to that of the initial two- or three-fold helical model in all simulations except Man3, the corresponding regular helix only constitutes a limited fraction of the configurations sampled along these simulations. Focusing on the eight main simulations, the corresponding occurences range from 2.0 to 33.8% (0.0% for Man3). These occurences increase if one includes quasi-regular helices (i.e. presenting one or a few linkages with θ values outside the expected range for a regular helix of the given type). For example, quasi-regular helices matching the initial helical structure except for at most one defect already account for 10.0 to 69.8% (0.1% for Man3) of the sampled configurations. Simulation Man3 evidences a marginal occurence of (quasi-)regular 3_2-helix (over the final 9 ns of the simulation), which is not surprising given that its dominant M value of 5 over this time period is incompatible with such a helix. However, when the comparison is performed relative to a 9_5-helix instead, the occurences of the regular helix and the quasi-regular helix with at most one defect raise to 37.4 and 68.0%, respectively.

The comparison of the different systems shows that simulations Gul2, Glc3 and (to a lesser extent) Gal2 sample configurations that are closer to their initial helical structures and simulations Glc2, Man2 and Man3 sample very different configurations, while simulations Gal3 and Gul3 show intermediate behaviour. These differences are also evidenced by the most frequently occuring distributions of linkages among local helical conformations. This distribution is encoded in Table 5 in the form of a pattern $a^{[']}bc^{[']}$ indicating how many linkages along the chain adopt a local 3_1-, 2_1- or 3_2-helical conformation, respectively (the prime corresponding to a linkage with θ outside any of the three corresponding intervals, its position indicating the closest recognised configuration). The leading patterns for Gul2 and Glc3 are the regular 2_1- and 3_2- helices, respectively, while the second and fourth or second and third most frequent patterns, respectively, are quasi-regular helices with a single defect. Simulations Gal2, Gal3 and Gul3 all have the regular helix (2_1-, 3_1- and 3_2-helix, respectively) as the third most frequent pattern, and the same helix with a single deffect as one of the two most frequent ones. In contrast, the leading patterns for Glc2 and Man2 are all irregular. For Man3, the analysis in terms of such patterns is probably somewhat misleading, since these do not account for the local 9_5-helical conformation.

Taken together, the above observations provide a hint that conformational ensembles in the neighbourhood of the regular 3_{2^-}, 9_{5^-}, 2_{1^-} and 2_1-helices may represent the expected helical propensities for single chain pGlcU, pManU, pGalU and pGulU, respectively, in solution, with the possibility of an alternative 3_1-helical form for pGalU.

The time evolution of the local helical conformation at the level of the N_{res} glycosidic linkages is illustrated in Figures 8 and 9 for the eight main simulations. The corresponding occurences and lifetimes, averaged over the N_{res} linkages (together with the associated standard deviations), are reported in Table 6 for all simulations. Note that local conformations that cannot be classified as 2_1-, 3_1- or 3_2- helical conformations (i.e. with θ outside the range [90; 270°]) have rather limited occurences, remaining below 1% except for simulations Glc3 (5.9%), Gal3 (7.8%), Gul3 (9.1%) and Man2H (2.8%).

Focusing on the eight main simulations, those initiated from a regular 2_1-helix expectedly show a predominance of local 2_1-helical conformations (66.1 and 57.5% for Glc2 and Man2; 81.4 and 85.0% for Gal2 and Gul2). However, local 3_1- and 3_2-helical conformations

Table 5. Occurences of regular (or quasi-regular) helices and most frequent distributions of the linkages among the different types of local helical conformations.

Code	H_0 (%)	H_1 (%)	H_2 (%)	H_3 (%)	P_1	P_2	P_3	P_4	P_5
Glc2	5.0	20.7	45.8	71.0	161 (20.9)	251 (18.9)	242 (15.4)	170 (11.9)	152 (6.1)
Man2	2.0	10.0	28.5	51.2	242 (25.3)	161 (15.4)	251 (15.1)	233 (10.1)	170 (7.3)
Gal2	20.5	53.9	82.5	95.0	170 (27.6)	161 (25.0)	080 (20.5)	251 (8.8)	071 (5.7)
Gul2	30.2	65.9	88.3	96.5	080 (30.2)	071 (23.2)	161 (19.9)	170 (12.5)	152 (4.4)
Glc3	33.8	69.8	90.8	97.8	009 (33.8)	018 (18.2)	008′ (17.9)	017′ (17.5)	026′ (3.5)
Man3	0.0	0.1	0.2	1.1	063 (30.2)	072 (29.2)	054 (11.3)	081 (8.4)	144 (7.5)
	0.5	9.0	38.2	69.6[a]					
	37.4	68.0	89.6	97.4[b]					
Gal3	14.8	46.4	76.3	92.9	810 (23.7)	7′10 (23.4)	900 (14.8)	6′20 (10.8)	8′00 (7.8)
Gul3	12.9	40.9	70.8	89.9	017′(24.1)	018 (20.1)	009 (12.9)	026′ (11.5)	008′ (7.9)
$Gul2_{Na}$	25.4	59.3	87.0	96.8	080 (25.4)	161 (25.1)	071 (20.6)	170 (13.4)	251 (4.9)
$Gul2_{LJ-}$	31.1	63.6	87.4	96.6	080 (31.1)	161 (21.5)	071 (18.8)	170 (13.6)	152 (5.2)
$Gul2_{LJ+}$	26.5	60.5	87.1	96.8	080 (26.5)	161 (24.2)	071 (20.5)	170 (13.5)	251 (4.9)
Glc2H	2.5	11.2	32.1	57.8	242 (20.4)	161 (18.5)	251 (14.9)	152 (10.0)	332 (7.3)
Man2H	0.1	0.7	4.7	14.8	242 (17.3)	323 (17.0)	233 (10.2)	332 (9.2)	314 (6.2)
Gal2H	9.8	31.6	61.3	83.6	161 (26.5)	170 (13.0)	251 (12.0)	242 (10.3)	080 (9.8)
Gul2H	9.6	31.1	61.3	84.0	161 (26.8)	071 (12.3)	251 (11.2)	152 (11.2)	242 (10.5)
$Gul2_{Na}H$	9.6	31.6	63.0	84.6	161 (27.7)	071 (12.9)	152 (11.1)	251 (10.2)	242 (10.0)

Note: The results are reported for the different simulations (Table 2). The successive entries H_k, $k = 0 \ldots 3$, denote the occurences of trajectory configurations where at least $N_{res} - k$ linkages are characterised by a turn angle θ in the appropriate range for the helical conformation of the regular helix used to initiate the corresponding simulation (Table 2). The successive P_k, $k = 1 \ldots 5$, entries encode the five most frequent distributions of the N_{res} residues among the different types of local helical conformations, together with the corresponding occurences (between parentheses; in percent). The first, second and third digits of the code denote the number of residues in a local 3_1-, 2_2- and 3_2- helical conformation, respectively. A prime after the first or third digit indicates the presence of one linkage with a θ value outside the range [90; 270°] respectively. The sum of the three digits increased by the number of primes is equal to N_{res}. See Section 2.2 for the definition of θ and of the associated local helical conformations. Averaging was performed over the final 9 ns of the simulations.[a] With reference to a regular 2_1-helix (instead of the 3_2-helical starting structure). [b] With reference to a regular 9_5-helix (instead of the 3_2-helical structure; a local 9_5-helical conformation is defined here by a turn angle θ within a range of $\pm 30°$ around 200°).

(which require a change of about $\pm 60°$ in θ) are also frequently encountered (about 15–20% each for Glc2 and Man2; about 5–10% each for Gal2 and Gul2). These alternative local conformations occur asynchronously and non-cooperatively along the chain (Figure 8), with average lifetimes of the order of 25–55 ps, except for the local 3_1-helical conformation in Man2 (181 ps; distinct formation events of about 1 ns duration are clarly visible in Figure 8, which coincide with the ϕ and θ transitions observed in Figure 5). The latter observation is probably related to the fact that the associated transition from the 2_1-helical conformation involves hopping between two non-overlapping wells of the ϕ distribution (Figure 4). The occurences of about 20% for the local 3_1-helical conformation in simulations Glc2 and Man2 agree very well with the populations associated with the minor peaks in the ϕ distributions (Section 3.2), the major peak being associated with all other local conformation (predominantly 2_1- and 3_2-helical).

Except for simulation Man3, the main simulations initiated from a regular three-fold (3_1- or 3_2-) helix show an even stronger predominance of the corresponding local helical conformation (87.9% for Glc3; 80.9 and 79.0% for Gal3 and Gul3, respectively). The alternative local 2_1-helical conformation (which requires a changes of about $\pm 60°$ in θ) is also frequently encountered (about 5–10%), but the local three-fold conformation of opposite handedness is essentially absent (probably because it requires a larger change of about $\pm 120°$ in θ). The alternative local 2_1-helical conformations also occurs asynchronously and non-cooperatively along the chain (Figure 9), withan average lifetime of the order of 30–45 ps. For simulation Man3 the results of Figure 9 and Table 6 are probably somewhat misleading, since they do not account for the local 9_5-helical conformation dominant after 1.02 ns.

The corresponding graphs describing the time-evolution of the local-helical conformation for the eight simulation variants are provided in Figures S.11 and S.12 (Suppl. Mat.). Expectedly, the interconversion between the different local helical conformations is much more rapid at 500 K compared to 300 K (Figure 8). Except for simulation Man2H, the average θ values are essentially unaltered (Table 4), the occurences of the three types of local helical conformations changes little (Table 6; by up to about 10%) and the populations of regular helices (Table 5) decrease by about a factor 2–3. The nature of the counter-ions for pGulU at 300 K has essentially no influence on any of the observables discussed in this section.

3.4 Intramolecular hydrogen bonding

The four homopolyuronates may present two types of inter-residue hydrogen bonds across the glycosidic linkage: $H_2 \rightarrow O'_6$ and $O_5 \leftarrow H'_3$ (Figure 2). Due to the

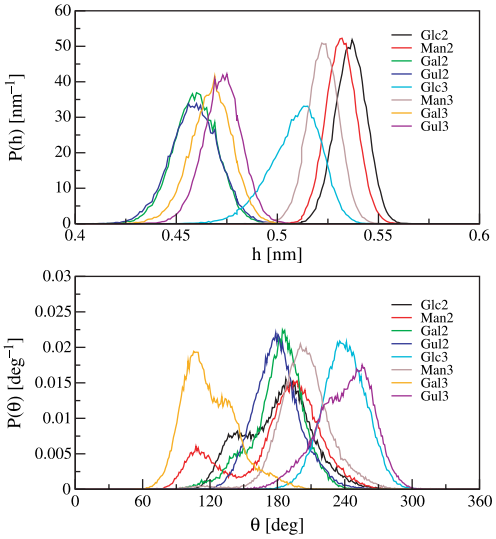

Figure 7. Normalised probability distributions of the helix raise h and turn angle θ, averaged over the N_{res} linkages, for the eight main simulations (300 K, Ca counter-ions; Table 2). See Section 2.2 for the definition of h and θ. Averaging was performed over the final 9 ns of the simulations.

axial orientation of the 2-OH group in pManU, the former hydrogen bond is incompatible with a regular 2_1-helical conformation (although it may occur in other conformations). Similarly, the orientation of the 3-OH group in pGulU prevents the formation of the second type of hydrogen bond in regular two- and three-fold helices. In an aqueous environment, the actual occurences of these inter-residue hydrogen bonds are expected to depend on the local chain conformation. In the solid state, where regular helices are observed, the reported crystallographic structures are compatible with $H_2 \rightarrow O'_6$ hydrogen bonds for pGlcU [18] (2_1-helix; presumed by analogy with the cellulose II structure [101]), pGalU [48] (3_1-helix) and pGulU [38–42] (2_1-helix), and with $O_5 \leftarrow H'_3$ hydrogen bonds for pGlcU [18] (2_1-helix; presumed) and pManU [38,39,42,50] (2_1-helix).

In the sixteen simulations, only the two above types of intramolecular hydrogen bonds were observed. The time evolution of these hydrogen bonds at the level of the N_{res} glycosidic linkages is illustrated in Figures 8 and 9 for the eight main simulations. The corresponding occurences and lifetimes, averaged over the N_{res} linkages

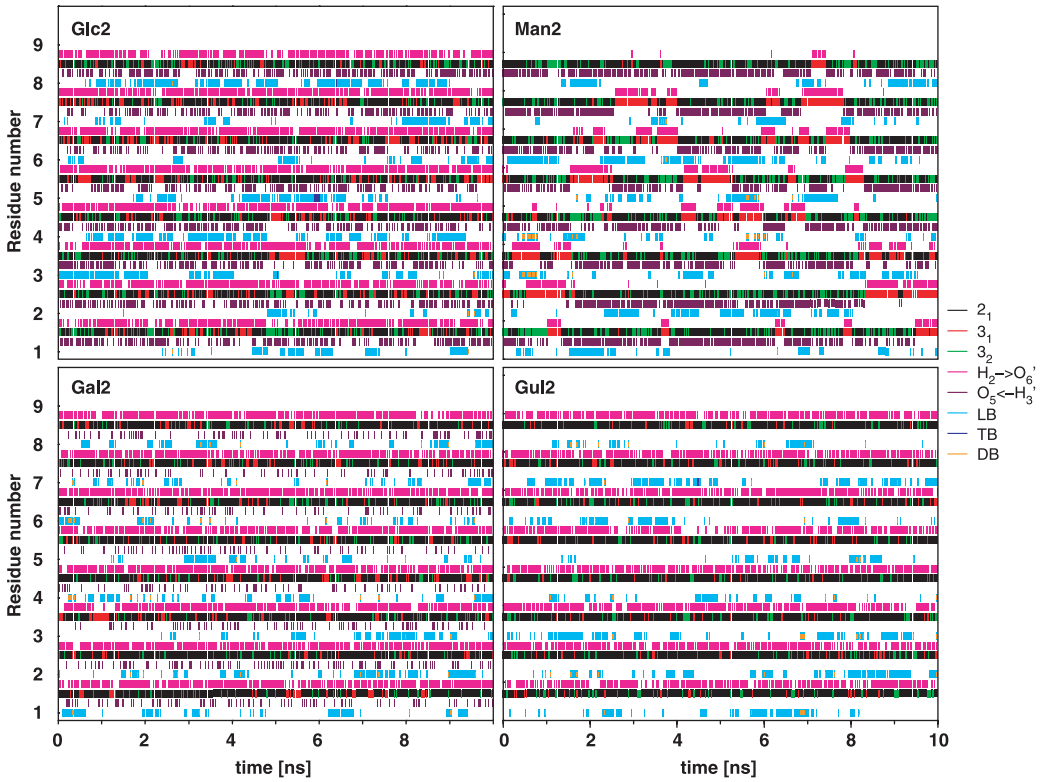

Figure 8. Time evolution of the local helical conformations and of the inter-residue hydrogen bonds for the N_{res} glycosidic linkages, as well as of ion binding events for the N_{res} residues, displayed for simulations Glc2, Man2, Gal2 and Gul2 (Table 2). The indicated events are the formation of a local 2_1 −, 3_1 − and 3_2-helical conformation, of ($H_2 \rightarrow O'_6$ or $O_5 \leftarrow H'_3$) hydrogen bonds, of a solvent-separated (loose binding; LB) ion pair, of a contact (tight binding; TB) ion pair or of an ion pair (LB or TB) involving an ion also bound (LB or TB) to the carboxylate group of another residue (double binding; DB; smaller bars for the two involved carboxylate groups). See Section 2.2 for definitions of local helical conformations, hydrogen bonding and ion binding. The sampling period (individual bars) is 20 ps. Colour code 2_1 (black), 3_2 (red), 3_2 (green), $H_2 \rightarrow O'_6$ (pink), $O_5 \leftarrow H'_3$ (brown), LB (cyan), TB (blue), DB (orange).

(together with the associated standard deviations), are reported in Table 6 for all simulations.

Focusing on the eight main simulations, the following qualitative observations can be made. The $H_2 \rightarrow O'_6$ hydrogen bond is only compatible (i.e. present with a significant occurence) with the following local helical conformations: 2_1 and 3_1 for pGlcU; 3_1 for pManU; 2_1, 3_2 and (to a limited extent) 3_1 for pGalU; 2_1 and (to a limited extent) 3_2 for pGulU. As a consequence of the populations of these local helical conformations in the different simulations, the occurence of the $H_2 \rightarrow O'_6$ hydrogen bond is high for Glc2, Gal2 and Gul2 (about 70–80%), moderate for Man2, Gal3 and Gul3 (about 20–25%), and low for Glc3 and Man3 (about 6% or less). The $O_5 \leftarrow H'_3$ hydrogen bond is only compatible with the following local helical conformations: 2_1 and (to a limited extent) 3_2 for pGlcU; 2_1 and (to a limited extent) 3_2 for pManU; 2_1 (to a limited extent) for pGalU; none for pGulU. As a consequence of the populations of these local helical conformations in the different simulations, the occurence of the $O_5 \leftarrow H'_3$ hydrogen bond is high for Glc2, Man2 and Man3 (about 45–75%), moderate for Gal2 and Glc3 (15–30%), and low for Gal3, Gul2 and Gul3 (about 3% or less). The lifetimes of the two types of hydrogen bonds range from 26 to 269 ps for the eight main simulation, the exact values being largely correlated with the corresponding occurences. The occurences of the two types of hydrogen bonds in simulations Glc2, Man2, Gal3 and Gul2 agree very well with the hydrogen bonding patterns suggested by the corresponding solid-state structures obtained from fibre diffraction measurements [18,38–42,48,50].

Assuming that intramolecular hydrogen bonding is an important conformational driving force, it is reasonable to expect that the formation of $H_2 \rightarrow O'_6$ inter-residue hydrogen bonds affects the rotameric distribution and isomerisation timescale of the γ angle characterising the orientation of the carboxylate groups (Section 3.1). However, the present simulations do not evidence clearly this presumed influence. In particular, the γ distribution is shifted by about 10° and becomes narrower for pGulU and pGalU when changing from an initial two-fold to an initial three-fold helical model (Figure 3), although the occurence of the $H_2 \rightarrow O'_6$ hydrogen bond concomittantly decreases (by about 50–55%). However, no similar change is seen in the γ distribution for pGlcU and pManU, although the occurence of this hydrogen bond also significantly decreases (by about 75 and 20%, respectively). Moreover, the rotational isomerisation timescale τ_γ is consistently at least an order of magnitude longer for pGlcU and pManU compared to pGalU and pGulU (Table 3), an observation that cannot be correlated with the occurences of the $H_2 \rightarrow O'_6$ hydrogen bond in the eight simulations.

The time evolution of the inter-residue hydrogen bonds for the eight simulation variants is illustrated in Figures S.11 and S.12 (Suppl. Mat.). Expectedly, the formation and disruption of hydrogen bonds is much more rapid at 500 K compared to 300 K (Figure 8). Surprisingly, however, the occurences of the two types of hydrogen bonds (Table 6) are not dramaticaly affected by the increase in temperature. A moderate decrease (by about 10–15%) is observed for both types of hydrogen bonds, except in simulation Man2H. The nature of the counter-ions for pGulU at 300 K has essentially no influence on inter-residue hydrogen bonding.

3.5 Ion binding

The radial distribution functions $g(\rho)$ between carboxylate oxygen atoms and the closest counter-ion, averaged over the N_{res} residues, are displayed in Figure 10 for all simulations (together with the corresponding integrals). Focusing on the twelve simulations involving Ca^{2+} counter-ions (at either 300 or 500 K), at least two density peaks can be seen in the neighbourhood of the carboxylate groups, centred at calcium–oxygen distances of 0.26 and 0.45 nm (at 300 K, a third peak is visible at 0.68 nm). These two first peaks correspond to contact (tight binding; TB) and solvent-separated (loose binding; LB) ion pairs. The two types of events are illustrated in Figure 11 (top) based on single frames extracted from the Gal2 simulation. For the two simulations involving Na^+ counter-ions, the corresponding peak positions are 0.23 and 0.44 nm (at 300 K, a third peak is visible at 0.64 nm). For the simulations performed using Ca^{2+}-like counter-ions with their effective radii decreased (increased) by 20%, the positions of these first two peaks are, as expected, shifted to lower (higher) distances relative to the standard Ca^{2+} ion. To quantify the occurences of LB and TB events, cutoff criteria were applied to the calcium–oxygen distance (Section 2.2), with cutoff values corresponding to the first and second minima in the $g(\rho)$ curves.

The occurences and lifetimes of LB and TB events, averaged over the N_{res} residues, are reported in Table 6 for all simulations. Maybe the most unexpected result of this analysis (see also Figure 10) is the very low occurences of TB events at 300 K ($<1\%$ for simulations Glc2 and $Gul2_{Na}$; none for the others). Although the sugar carboxylate groups are commonly found in the second solvation shells of the counter-ions at this temperature (LB; occurences of about 25–30%), they almost never penetrate into their first solvation shells.

The two simulations with Ca^{2+}-like counter-ions were undertaken to ascertain that this observation was not the consequence of an improper choice of ion-solvent Lennard-Jones interaction parameters, since there is room

Table 6. Local helical conformations, intramolecular hydrogen bonding and ion binding.

Code	2_1	3_1	3_2	$H_2 \rightarrow O_6'$	$O_5 \rightarrow H_3'$	LB	TB	DB
Occurences (%)								
Glc2	66.1 (2.9)	19.3 (4.6)	14.6 (3.8)	79.2 (4.9)	45.9 (3.7)	31.9 (15.2)	0.3 (0.5)	0.3 (0.2)
Man2	57.5 (5.4)	20.7 (7.1)	20.8 (2.9)	19.5 (6.8)	55.9 (5.7)	26.4 (7.2)	–	1.2 (0.7)
Gal2	81.4 (2.7)	11.4 (2.1)	7.2 (1.1)	80.0 (1.4)	17.9 (1.8)	23.4 (5.1)	–	1.5 (0.7)
Gul2	85.0 (1.4)	6.7 (1.2)	8.2 (1.4)	69.5 (2.5)	–	27.1 (9.1)	–	2.4 (0.7)
Glc3	6.1 (1.2)	–	87.9 (1.9)	5.9 (1.5)	28.3 (3.9)	25.5 (7.3)	–	4.1 (1.5)
Man3	66.2 (3.0)	2.0 (2.1)	31.6 (3.9)	1.6 (1.8)	74.7 (1.7)	30.2 (9.8)	–	0.7 (0.9)
Gal3	11.2 (3.6)	80.9 (1.8)	–	26.2 (5.5)	2.6 (0.8)	25.6 (6.8)	–	3.9 (2.7)
Gul3	11.9 (3.8)	–	79.0 (2.6)	21.8 (5.7)	–	29.3 (7.8)	–	6.3 (2.3)
$Gul2_{Na}$	83.5 (1.4)	7.7 (1.1)	8.7 (0.8)	68.3 (3.1)	–	28.5 (7.5)	0.6 (1.0)	4.1 (3.3)
$Gul2_{LJ-}$	84.8 (1.9)	7.1 (1.4)	8.1 (1.4)	68.5 (1.3)	–	28.5 (13.4)	–	1.3 (0.8)
$Gul2_{LJ+}$	83.7 (1.9)	7.6 (1.5)	8.6 (1.7)	68.0 (2.2)	–	28.6 (3.7)	–	4.3 (1.7)
Glc2H	59.8 (1.2)	20.8 (1.6)	18.9 (1.2)	71.9 (1.4)	34.0 (0.9)	34.8 (3.0)	7.9 (2.3)	1.9 (0.6)
Man2H	37.7 (1.2)	28.8 (2.3)	30.7 (2.4)	25.3 (2.1)	24.8 (0.9)	41.2 (4.6)	13.2 (4.2)	6.6 (0.8)
Gal2H	72.6 (1.0)	14.2 (0.8)	13.0 (0.9)	66.9 (0.8)	17.3 (0.6)	38.8 (2.3)	7.9 (1.7)	6.3 (0.8)
Gul2H	72.6 (0.9)	1.5 (0.9)	13.8 (0.8)	60.7 (1.1)	–	37.4 (4.9)	7.6 (2.7)	5.3 (0.9)
$Gul2_{Na}H$	73.0 (1.1)	13.2 (0.7)	13.7 (0.8)	61.3 (1.1)	–	35.6 (2.0)	7.2 (0.9)	5.5 (0.6)
Lifetime (ps)								
Glc2	143 (26)	55 (9)	38 (6)	269 (56)	100 (13)	146 (28)	21 (46)	19 (8)
Man2	172 (44)	181 (66)	47 (6)	177 (41)	220 (50)	122 (27)	–	34 (18)
Gal2	318 (93)	44 (8)	26 (2)	234 (26)	34 (3)	93 (23)	–	29 (8)
Gul2	448 (64)	25 (3)	31 (7)	167 (15)	–	100 (19)	–	32 (6)
Glc3	28 (4)	–	1097 (418)	25 (4)	77 (12)	99 (21)	–	40 (10)
Man3	190 (26)	51 (47)	50 (8)	56 (53)	444 (107)	129 (17)	–	17 (14)
Gal3	46 (6)	361 (89)	–	54 (7)	26 (3)	101 (28)	–	48 (13)
Gul3	39 (5)	–	303 (57)	43 (4)	–	103 (34)	–	46 (10)
$Gul2_{Na}$	405 (76)	29 (5)	33 (3)	175 (25)	–	70 (14)	25 (49)	39 (12)
$Gul2_{LJ-}$	399 (88)	28 (4)	30 (5)	164 (23)	–	154 (58)	–	23 (13)
$Gul2_{LJ+}$	428 (52)	26 (2)	31 (4)	160 (12)	–	93 (20)	–	40 (13)
Glc2H	211 (26)	32 (1)	30 (1)	336 (98)	60 (3)	67 (10)	50 (9)	21 (5)
Man2H	58 (3)	48 (5)	51 (7)	47 (4)	49 (4)	76 (9)	59 (16)	27 (4)
Gal2H	524 (141)	24 (1)	25 (2)	522 (116)	33 (3)	64 (6)	46 (5)	23 (4)
Gul2H	748 (267)	25 (1)	25 (2)	322 (56)	–	62 (8)	48 (11)	22 (3)
$Gul2_{Na}H$	738 (161)	24 (1)	24 (1)	314 (48)	–	45 (3)	24 (3)	21 (2)

Note: The occurences and lifetimes of local helical conformations, intramolecular hydrogen bonds (only observed to occur between adjacent residues) and ion binding, averaged over the N_{res} linkages (two former types of observables) or the N_{res} residues (binding events) are reported together with the corresponding standard deviations over the N_{res} individual values (indicated between parentheses) for the different simulations (Table 2). The indicated properties are the formation of a local 2_1-, 3_1- or 3_2-helical conformation, of ($H_2 \rightarrow O_6'$ and $O_5 \rightarrow H_3'$) hydrogen bonds, of a solvent-separated (loose binding; LB) ion pair, of a contact (tight binding; TB) ion pair, or of an ion pair (LB or TB) involving an ion also bound (LB or TB) to the carboxylate group of the another residue (double binding; DB). The percentages of the three local helical conformations do not add up to 100%, due to the (limited) occurrence of other conformations (with θ outside the range [90; 270°]). These other conformations also influence the lifetimes of the three conformations. See Section 2.2 for the definitions of local helical conformations, hydrogen bonding and ion binding. Averaging was performed over the final 9 ns of the simulations.

for ambiguity concerning the appropriate way to calibrate these parameters [102,103]. However, the use of a Ca^{2+}-like ion with its effective radius decreased or increased by 20% did not change the above picture qualitatively. The simulations also failed to evidence any striking qualitative difference between the coordination of Ca^{2+} and Na^+ in terms of $g(\rho)$ and TB events, in spite of the different ionic charge.

A second counter-intuitive observation is that an elevated temperature of 500 K enhances ionic binding, in spite of the increased thermal motion (the occurences of LB and TB events increasing from about 25–30% and 0%, respectively, to about 35–40% and 8–13%, respectively). This observation is probably related to the decrease in the dielectric permittivity of water upon increasing the temperature, leading to a reduction of solvation effects. Since dielectric screening opposes favorable electrostatic interactions between carboxylate groups and counter-ions, this is expected (and observed) to induce a tighter binding of the counter-ions to the chain. Independent simulations of a pure SPC water system (data not shown) evidenced a decrease in the premittivity (evaluated using the appropriate dipole-moment fluctuation formula [84]) from 61 to 34 upon increasing the temperature from 300 to 500 K. Experimentally, the permittivity of water decreases from 78.3 to 55.7 upon increasing the temperature from 298.15 to 398.15 K [104]. Such an attenuation of dielectric screening upon increasing the temperature, leading to an enhanced influence of direct solute-solute or solute-ion electrostatic interactions, has been evidenced previously [105].

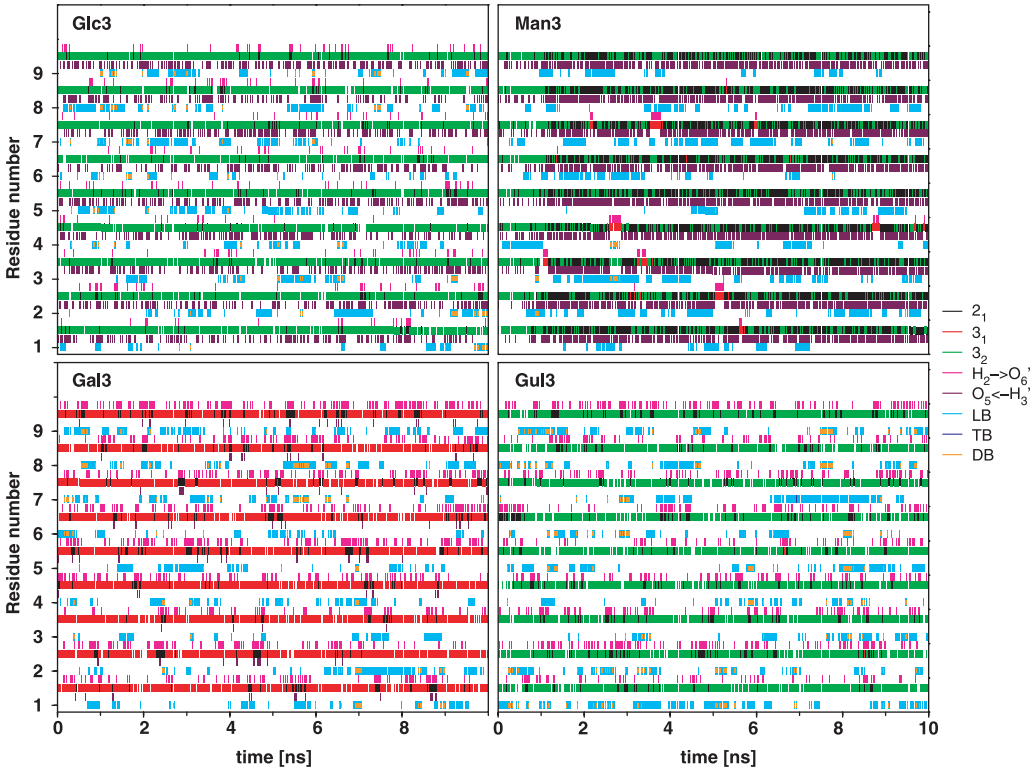

Figure 9. Time evolution of the local helical conformations and of the inter-residue hydrogen bonds for the N_{res} glycosidic linkages, as well as of ion binding events for the N_{res} residues, displayed for simulations Glc3, Man3, Gal3 and Gul3 (Table 2). The indicated events are the formation of a local 2_1-, 3_1- or 3_2-helical conformation, of ($H_2 \rightarrow O'_6$ or $O_5 \leftarrow H'_3$) hydrogen bonds, of a solvent-separated (loose binding; LB) ion pair, of a contact (tight binding; TB) ion pair or of an ion pair (LB or TB) involving an ion also bound (LB or TB) to the carboxylate group of another residue (double binding; DB; smaller bars for the two involved carboxylate groups). See Section 2.2 for definitions of local helical conformations, hydrogen bonding and ion binding. The sampling period (individual bars) is 20 ps. Colour code 2_1 (black), 3_1 (red), 3_2 (green), $H_2 \rightarrow O'_6$ (pink), $O_5 \leftarrow H'_3$ (brown), LB (cyan), TB (blue), DB (orange).

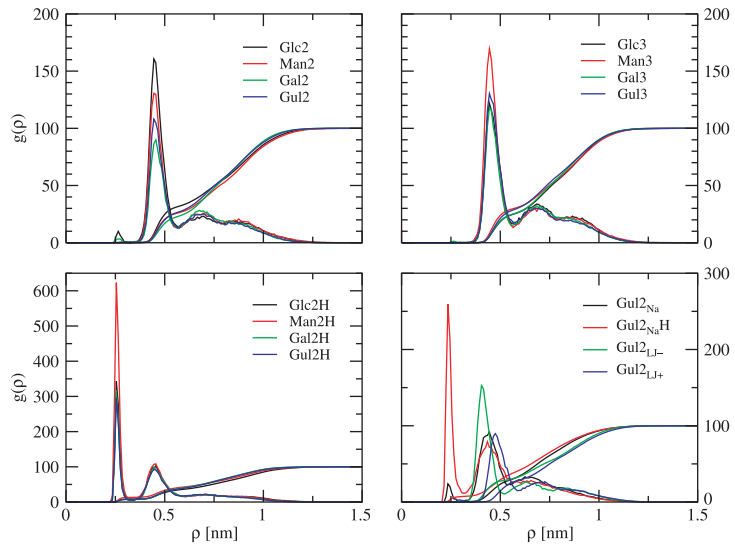

Figure 10. Radial distribution function $g(\rho)$ for the smallest (minimum-image) distance between any of the two carboxylate oxygen atoms of a given residue and the closest positive counter-ion, averaged over the N_{res} residues, for the different simulations (Table 2). The cummulative integral of $V^{-1} 4\pi\rho^2 g(\rho)$ (amplified by 100 for readability) is also displayed. See Section 2.2 for the definitions of $g(\rho)$ and V. Averaging was performed over the final 9 ns of the simulations.

The lifetimes of LB events are of the order of 100–150 ps for Ca^{2+} (70 ps for Na^{+}) at 300 K, and somewhat shorter (60–70 ps) for Ca^{2+} (similar for Na^{+}) at 500 K. The lifetimes of TB events are about 20 ps for both Ca^{2+} and Na^{+} at 300 K, and somewhat longer for Ca^{2+} (about 50–60 ps) and Na^{+} (about 25 ps) at 500 K.

Double binding (DB; ion bridging) events (i.e. carboxylate groups binding an ion that is simultaneously bound to the carboxylate group of another residue) were relatively unfrequent during the simulations, the corresponding occurences ranging from 0.3 to 6.3% (with lifetimes of the order of 20–50 ps) for the main simulations (Table 6). These occurences also slightly increased when raising the temperature from 300 to 500 K. Triple binding events (Ca^{2+} bound to three carboxylate groups) were observed but with negligible occurences (<0.3% in all simulations). All DB events were found to involve either neighbour (DB_n) or second-neighbour (DB_s) residues along the chains. Illustrations for those types of events are provided in Figure 11 (bottom). At 300 K, DB_n events represented the leading contribution to DB events for simulations Glc2 and Man2 (80–90%), as well as for all simulations initiated from a three-fold helical model (95–99%). In contrast, DB_s events were more frequent in simulations Gal2 and Gul2 (80–85%). These differences are probably related to differences in the preferred values for the local turn angle and helix raise (determining the spatial proximity between neighbour and second-neighbour carboxylate groups) and in the glycosidic linkage flexibility (e.g. DB_n events in a 2_1-helix must be associated with a significant distortion of the local helical conformation; Figure 11).

The time evolution of calcium binding events is illustrated in Figures 8 and 9 as well as S.11 and S.12 (Suppl. Mat.) for all simulations. These graphs do not reveal any obvious correlation between ion binding events, local helical conformation and inter-residue hydrogen bonding. Note also that since TB and DB events have so limited occurrences at 300 K, it is unlikely that calcium binding has a significant influence on the conformational preferences and rotational isomerisation timescale of the carboxylate groups (Section 3.1).

The distributions of the positive counter-ions around the chains (sampled at 10 ps intervals along the trajectories, excluding the initial 1 ns of the simulations), are illustrated in Figure 12 for the eight main simulations. Analogous illustrations for the simulation variants are provided in Figure S.13 (Suppl. Mat.). The associated two-dimensional radial distribution functions $g_{2D}(r)$ for the ion coordinates in the *xy*-plane relative to the helix axis are provided in Figure S.14 (Suppl. Mat.) for all simulations. These figures further point towards a lack of specific binding of the counter-ions to the chain, irrespective of the system considered (polyuronate type, initial helical model, temperature and nature of the counter-ions). In all cases, the counter-ion atmosphere is almost entirely confined to a cylindrical region around the chain axis. Although the counter-ion density within this region exhibits some broad patterns, the absence of well-defined binding sites remains evident. For the Ca^{2+} and Ca^{2+}-like ions, the cylinder radii accounting for 95% (or 99%) of the counter-ion density range from 1.0 to 1.1 (or 1.1 to 1.2) nm irrespective of the temperature. For the Na^{+} ions, the counter-ion atmosphere is slightly more diffuse, but 90% of the counter-ion density is still contained within cylinders of 1.8 (300 K) and 2.2 (500 K) nm radii. Note that the observed confinement could possibly be enhanced by the artificial periodicity of the system in the *xy*-plane (i.e. the chains are surrounded in this plane by an infinite lattice of periodic replicas with a spacing of about 5 nm; Table 2). However, the absence of visible anisotropy in the counter-ion distributions (with the possible exception of simulations $Gul2_{Na}$ and $Gul2_{Na}H$) and the nearly complete charge cancellation after a distance of about 1.2 nm (for Ca^{2+} and Ca^{2+}-like ions; effectively excluding the presence of long-range electrostatic interactions between the screened chain and its periodic copies) suggest that this effect is not significant. A change in temperature from 300 to 500 K promotes a slight contraction of the counter-ion atmosphere around the chain, in agreement with the previous observations concerning LB, TB and DB events. The corresponding peak positions in $g_{2D}(r)$ are shifted to lower values by about 0.15 nm for both Ca^{2+} and Na^{+} counter-ions. Finally, it should be stressed that all the above observations are in principle restricted to the counter-ion concentration ranges and solution ionic strengths investigated in the present simulations (neutralising amount; no other salt in solution).

The fact that the counter-ions do not show strong binding to the carboxylate groups renders a tight interaction with the other sugar oxygen atoms unlikely. Radial distribution functions for the distances between the oxygen atoms O_1 (glycosidic oxygen), O_2 and O_3 (hydroxyl groups), or O_5 (ring oxygen) and the closest counter-ion are displayed in Figures S.15–S.18 (Suppl. Mat.) for all simulations. The corresponding occurences of LB and TB events, based on appropriate cutoff criteria (Section 2.2), are reported in Table S.2 (Suppl. Mat.). Focusing on the eight main simulations, LB events are infrequent (at most about 15%) and TB events exceptional (<2% for simulations Glc3 and Gul3; none for the others). At 500 K, the occurences of LB events increase to about 10–20% while those of TB events remain very low. The glycosidic oxygen and, to a lesser extent, the ring oxygen atoms appear to present a somewhat lower affinity for the counter-ions compared to the two hydroxyl oxygen atoms. Finally, Na^{+} is seen

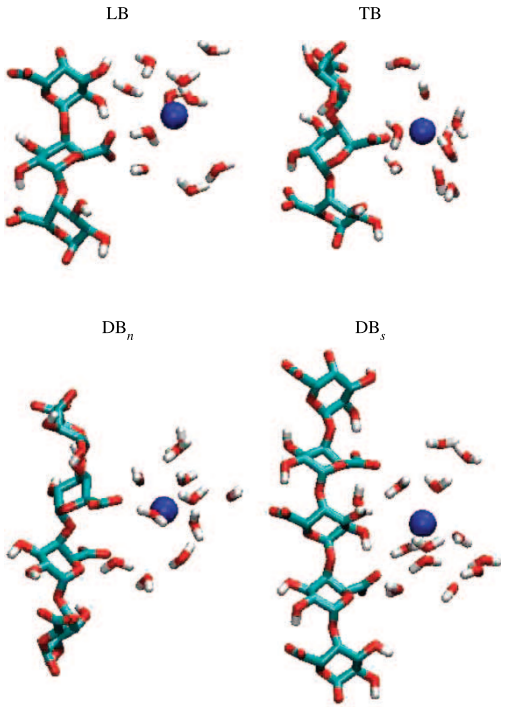

Figure 11. Snapshots from the Gal2 simulation. The configurations illustrate the following events: loose binding (LB; $t = 1.664$ ns, residues 3–5, $\rho = 0.43$ nm); tight binding (TB; $t = 5.700$ ns, residues 2–4, $\rho = 0.26$ nm); double binding involving neighbour residues (DB$_n$; $t = 3.859$ ns, residues 1–4, $\rho = 0.46$ and 0.50 nm relative to the carboxylate groups of residues 2 and 3, respectively); double binding involving second-neighbour residues (DB$_s$; $t = 4.094$ ns; residues 4–8, $\rho = 0.50$ and 0.48 nm relative to the carboxylate groups of residues 4 and 7, respectively). The orientation (top to bottom of each drawing) is from the non-reducing to the reducing end. Only water molecules with their oxygen atoms closer than 0.6 nm from the counter-ion are displayed.

to have a slightly higher propensity for coordination to the sugar oxygen atoms compared to Ca^{2+}.

3.6 *Diffusion properties*

The mean-square displacements Q_z, Q_{xy} and Q_Θ associated with the chain longitudinal, transverse and rotational rigid-body motions are displayed in Figure S.19 (Suppl. Mat.) in the form of averages over different sets of simulations. The mean-square displacements $Q_{i,z}$ and $Q_{i,xy}$ associated with the counter-ion coordinates along the z-axis and in the xy-plane, averaged over the N_{ion} positive ions, are displayed in Figure S.20 (Suppl. Mat.) in the same form. The corresponding diffusion coefficients D_z, D_{xy}, D_Θ, $D_{i,z}$ and $D_{i,xy}$ are reported in Table 7, while the values calculated for all individual simulations are provided in Table S.3 (Suppl. Mat.). However, because the individual mean-square-displacement curves significantly deviated from linearity the latter values may not be well converged. For this reason, the results are only discussed here in terms of averages over four sets of simulations: (i) all simulations at 300 K with Ca^{2+} counter-ions; (ii) the corresponding simulations initiated from a 2_1-helical structure; (iii) the corresponding simulations initiated from a three-fold (3_1- or 3_2-) helical structure; (iv) all simulations at 500 K with Ca^{2+} counter-ions.

The mean-square displacement curves averaged over the four above sets of simulations were found to be essentially linear over the interval from 0 to 3 ns, with the possible exception of the transverse mean-square displacement $Q_{i,xy}$ of the ions. Here, the curves showed sublinear (non-Einstein) behaviour, especially visible at

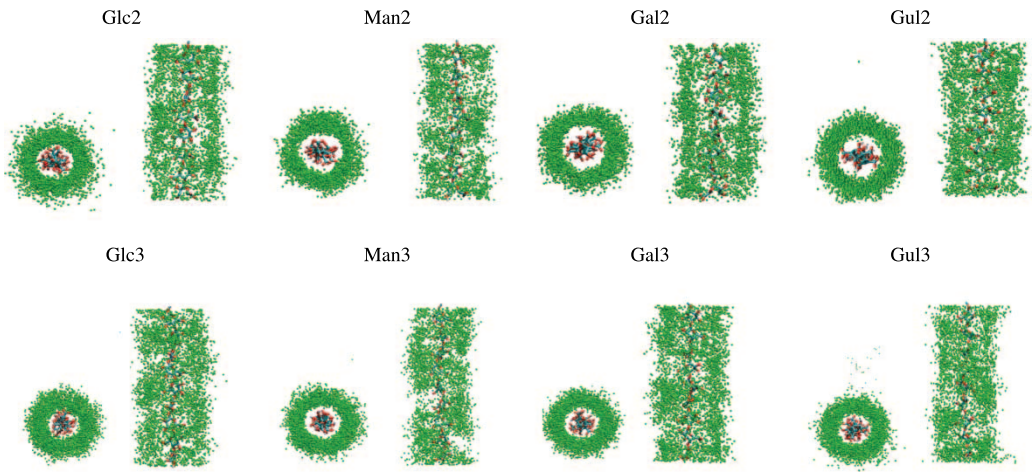

Figure 12. Positions of the counter-ions along the chain (top and side views), as sampled along the eight main simulations (300 K, Ca^{2+} counter-ions; Table 2). The ion coordinates correspond to successive configurations superimposed onto the initial (after 0.2 ns equilibration) one (rotational and translational fit based on the C_2, C_3, C_5 and O_5 atoms). The latter reference configuration is also displayed. The sampling period (between displayed ion coordinates) is 10 ps. The figures correspond to the final 9 ns of the simulations.

500 K. This is probably a consequence of the confinement of the counter-ion atmosphere to a cylindrical region around the chain (Section 3.5).

Focusing on the eight main simulations, the diffusion coefficients D_z, D_{xy} and D_Θ associated with the chain rigid-body motion at 300 K are 0.85 $nm^2\,ns^{-1}$, 0.38 $nm^2\,ns^{-1}$ and 2.45 $deg^2\,ns^{-1}$. Expectedly, the chain diffuses faster along its axis than transversally (by about a factor of two), which is related to the larger effective cross-section (exposed to solvent-induced friction) associated with the latter type of motion. The corresponding expected (root-mean-square) displacements over the 10 ns simulations are 4.1 nm, 3.9 nm (the corresponding expected displacements along x or y separately are 2.8 nm) and 7.0°. When comparing the sets of simulations initiated from two- and three-fold helices at 300 K, it appears that the former chains are somewhat more diffusive in all three degrees of freedom compared to the latter ones (by about 20–40%). This observation is probably related to the larger effective cross-section associated with three-fold helices compared to their two-fold analogues. Finally, as expected, the chain diffusion for pGulU (2_1-helix) is significantly faster at 500 K (by about a factor 3–7).

Again focusing on the main simulations, the average diffusion coefficients $D_{i,z}$ and $D_{i,xy}$ associated with the longitudinal and transverse motions of the counter-ions are 0.43 and 0.19 $nm^2\,ns^{-1}$. The latter value is somewhat uncertain because the mean-square displacement is sublinear in time (see above). This observation, together with the comparison of the two numbers suggests that the ions diffuse normally along the chain axis, while they are restricted in their transverse motion by confinement within the counter-ion atmosphere. The differences between the sets of simulations initiated from two- and three-fold helices at 300 K are probably not significant. Finally, although the longitudinal diffusion of the counter-ions around pGulU (2_1-helix) is significantly faster at 500 K (by about a factor 3), the opposite is true for the transverse diffusion (reduced by about a factor 3). The reasons for these two observations are probably the enhanced thermal motion (increase in $D_{i,z}$) and the contraction of the counter-ion atmosphere around the chain (decrease in $D_{i,xy}$) at elevated temperature. The latter effect is particularly visible in the corresponding mean-square displacement curve at 500 K, which reaches a plateau value of 1 nm^2 (comparable with the approximate square radii of the confinement cylinders; see above) after about 0.5 ns, implying that at this temperature, the ions are essentially unable to escape the close neighbourhood of the chain (Section 3.5).

4. Conclusions

It is important to realise that the present simulations account for a somewhat 'unphysical' situation (even at 300 K in the presence of Ca^{2+} or Na^+ counter-ions). Because artificial periodicity is applied along the chain axis based on repeat units (8 or 9 residues) that are significantly shorter than the persistence lengths of the polymers expressed on a per residue basis (about 20 for pGlcU and pManU; about 40 for pGalU and pGulU), it enforces an increased extent of regularity compared to the experimental situation. Furthermore, the consideration of single chains excludes the possibility of dimer formation, which would occur experimentally in the presence of Ca^{2+} counter-ions at the concentration considered. In this sense, the simulations probe locally ordered states that may transiently exist (with limited equilibrium populations) within more disordered chains in the aqueous environment. However, the consideration of these more ordered states is justified by the fact that these are likely to represent the productive conformations for chain–chain association in junction zones and the formation of gels.

The main conclusions of the present study can be summarised as follows:

A. Although regular helical structures, as inferred from fibre diffraction measurements in the solid state [18,38–43,48,50] or built using molecular modelling procedures [19,51] are useful conceptual models,

Table 7. Diffusion constants evaluated for different sets of degrees of freedom of the chain and of the counter-ions.

D_q	300 K (all)	300 K (2-fold)	300 K (3-fold)	500 K (2-fold)
D_z ($nm^2 \cdot ns^{-1}$)	0.85 (0.29)	0.92 (0.64)	0.78 (0.24)	3.26 (2.30)
D_{xy} ($nm^2 \cdot ns^{-1}$)	0.38 (0.07)	0.44 (0.13)	0.31 (0.07)	1.44 (0.51)
D_Θ ($deg^2 \cdot ns^{-1}$)	2.45 (0.55)	2.68 (0.75)	2.21 (1.02)	18.12 (5.23)
$D_{i,z}$ ($nm^2 \cdot ns^{-1}$)	0.41 (0.09)	0.41 (0.12)	0.40 (0.18)	3.02 (1.99)
$D_{i,xy}$ ($nm^2 \cdot ns^{-1}$)	0.19 (0.05)	0.14 (0.02)	0.24 (0.10)	0.05 (0.01)

The results (together with error estimates; between parentheses) are reported in the form of averages over different sets of N_{sim} simulations (Table 2). The diffusion coefficients D_q are calculated from a linear least-square-fit of the corresponding mean-square displacements $Q_q(t)$ over the time period from 0 to 3 ns. The chain diffusion is described in terms of the longitudinal (D_z), transverse (D_{xy}) and rotational (D_Θ) diffusion constants. The ionic diffusion is described in terms the ionic longitudinal ($D_{i,z}$) and transverse ($D_{i,xy}$) diffusion constants, averaged over the N_{ions} positive counter-ions. The error estimate corresponds to the standard deviation of the calculated values over the N_{sim} simulations divided by $(N_{sim} - 1)^{1/2}$. The simulation sets correspond to all simulations at 300 K with Ca^{2+} counter-ions ($N_{sim} = 8$), those started from two-fold ($N_{sim} = 4$) or three-fold ($N_{sim} = 4$) helical structure, or all simulations at 500 K with Ca^{2+} counter-ions ($N_{sim} = 4$; pGulU; initiated from a two-fold helical structure). See Section 2.2 for the definition of $Q_q(t)$ and D_q. The calculation was performed considering the final 9 ns of the simulations and all possible time origins.

they may represent a rather misleading picture of the complex conformational ensembles populated by single polyuronate chains in aqueous solution. The present simulations reveal an important conformational flexibility (in time) and variability (along the chain) for the glycosidic linkages and local helical parameters. Conformations in the appropriate range for being classified as regular helices only account for a limited fraction of the sampled configurations ($\leq 35\%$, and the helicity of the chain fluctuates locally (*i.e.* non-cooperatively) on a timescale ranging from 20 ps to 1 ns. The extent of regularity is likely to be even more limited in the absence of the (artificial) periodicity constraint employed in the present simulations, as suggested by other modelling studies using Monte Carlo sampling of the accessible glycosidic linkage conformations for long polymer chains [19,51,53].

B. The binding of counter-ions to the polyuronate single chains appears to be largely non-specific irrespective of the type of polyuronate, choice of initial helical model, nature of the counter-ions and temperature. The counter-ion atmosphere is almost entirely confined within a cylinder of high ionic density around the chain axis. No well defined binding sites can be identified, and the differences observed in the modelling study of Braccini et al. [51] between diequatorially- and diaxially-linked polyuronate single chains in terms of ion binding are not reproduced in the present simulations. At 300 K, the carboxylate groups frequently (about 25–30% occurences) bind counter-ions, but nearly always remain in their second solvation shells. Events of tight binding, as well as of multiple coordination, are scarce and of short durations. These findings are in line with recent theoretical models suggesting that counter-ion binding to polyuronate single chains is (predominantly) a (non-specific) counter-ion condensation process [17,65–67]. In the present simulations, the counter-ion atmosphere leads to a nearly complete cancellation of the polymer charge within about 1.2 nm of the chain axis (charge reversal could possibly occur at higher counter-ion concentrations). This charge cancellation may significantly accelerate the kinetics of dimer formation by removal of the long-range Coulombic repulsion between the chains. Interestingly, an increase of the temperature to 500 K promotes a contraction of the counter-ion atmosphere and an increase in the occurences of tight binding and double binding events, presumably through a decrease of the solvent permitivitty (reduced dielectric screening).

C. The simulations suggest that the helical propensities for single-chain homopoly-uronates in aqueous solution are 3_2- (pGulU), $9_5/2_1$- (pManU), 2- (pGalU) and 2_1- (pGulU) helices, with the possibility of an alternative 3_1-helix for pGalU. These forms are representative (in an average sense; see point A) for the conformational ensembles probed by theose of the present simulations at 300 K showing the highest extent of regularity. Although probably associated with limited equilibrium populations in long polyuronate chains, these helical forms may still represent the productive conformations for chain–chain association. Indeed, the suggested helical propensities for pGulU and pGalU are conform with the most popular structural models for junction zones in pectin and alginate gels [13,28,30,32–34,41].

D. Intramolecular hydrogen bonding exclusively involves $H_2 \rightarrow O'_6$ and $O_5 \leftarrow H'_3$ hydrogen bonds across the glycosidic linkages, for all systems considered. Their occurences in the simulations initiated from the different helical structures agree very well with the hydrogen bonding patterns suggested by the corresponding solid-state structures obtained from fibre diffraction measurements [18,38–42,48,50]. These two hydrogen bonds can only be realised for specific local helical conformations at the level of the corresponding glycosidic linkage (which depend on the type of polyuronate). On the sole basis of the present simulations, it remains difficult to assess whether intramolecular hydrogen bonding represents a major driving force in determining the conformational preferences of the glycosidic linkages, or rather an 'opportunistic' consequence of the favorable positioning of two groups given a specific linkage conformation (itself predominantly determined by steric and stereoelectronic effects), as has been suggested to be generally the case for carbohydrates in an aqueous environment [78].

Two main features of polyuronate single chains revealed by the present study, namely the important extent of irregularity and conformational flexibility (point A) and the absence of well defined counter-ion binding sites (point B), take a special significance if one compares them to the models proposed for chain–chain association (e.g. egg-box model [29,32] and more recent alternatives [34,35,41,42,45–47]). In these models, two chains associate in rigid and regular helical conformations providing specific sites for the chelation of calcium ions via contact (tight binding) interaction with two carboxylate groups and a number of sugar hydroxyl groups from the two chains (without the involvment of water molecules). If the main features of these models are correct, the observations made in the present study suggest that chain–chain association within junction zones must be accompanied by a substantial stiffening of the chains and a dramatic change in the ion binding mode.

A possible interpretation of this process is the following. The tight binding of a calcium ion (contact ion pair, *i.e*. including partial desolvation) is an energetically unfavorable process when a single carboxylate group is involved. It requires an interaction with two carboxylate groups that are optimally positioned and oriented (and probably also the assistance of sugar hydroxyl groups). Single-chain polyuronates are unable to provide such a geometry (or only at the expense of a too demanding conformational entropy decrease), and the counter-ions remain bound in a non-specific way within a dense counter-ion atmosphere. However, the counter-ion charges are not locally compensated and the ionic atmosphere is associated with an important (positive) self energy due to the Coulombic repulsion between the counter-ions. In other words, the calcium ions around the single chain can be viewed as being placed in a 'reactive' state. The possibility of forming an appropriate chelating environment (involving a local compensation of the counter-ion charges and thus, the effective removal of inter-ionic repulsions) by association of a second polyuronate chain is likely to represent the leading driving force (in addition to presumably weaker direct chain–chain interactions) permitting chain stiffening, cation imobilisation and chain–chain association.

Acknowledgements

Financial support by the Swiss National Foundation, grant #21-105397, is gratefully acknowledged.

References

[1] Y.S. Ovodov, *Structural chemistry of plant glycuronoglycans*, Pure. Appl. Chem. 42 (1974), p. 351.
[2] D.A. Rees and E.J. Welsh, *Secondary and tertiary structure of polysaccharides in solutions and gels*, Angew. Chem. Int. Ed. Engl. 16 (1977), p. 214.
[3] E.R. Morris, *Molecular interactions in polysaccharide gelation*, Brit. Polym. J. 18 (1986), p. 14.
[4] D.A. Rees, *Polysaccharide shapes and their interactions-some recent advances*, Pure Appl. Chem. 53 (1981), p. 1.
[5] H.P. Ramesh and R.N. Tharanathan, *Carbohydrates. The renewable raw materials of high biotechnological value*, Crit. Rev. Biotech. 23 (2003), p. 149.
[6] O. Smidsrod and K.I. Draget, *Chemistry and physical properties of alginates*, Carbohydr. Eur. 14 (1996), p. 6.
[7] B.R. Thakur, R.K. Singh, and A.K. Handa, *Chemistry and uses of pectin - a review*, Crit. Rev. Food Sci. Nut. 37 (1997), p. 47.
[8] B.L. Ridley, M.A. O'Neill, and D. Mohnen, *Pectins: structure, biosynthesis, and oligogalacturonide-related signaling*, Phytochemistry 57 (2001), p. 929.
[9] W.G.T. Willats et al., *Pectin: cell biology and prospects for functional analysis*, Plant Mol. Biol. 47 (2001), p. 9.
[10] S Pérez, K. Mazeau, and C Herve du Penhoat, *The three-dimensional structures of the pectic polysaccharides*, Plant Physiol. Bioch. 38 (2000), p. 37.
[11] M.D. Walkinshaw and S. Arnott, *Conformations and interactions of pectins II: models for junction zones in pectinic acid and calcium pectate gels*, J. Mol. Biol. 153 (1981), p. 1075.
[12] D.A. Powell et al., *Conformations and interactions of pectins II: influence of residue sequence on chain association in calcium pectate gels*, J. Mol. Biol. 155 (1982), p. 517.
[13] D.A. Rees, *Polysaccharide conformation in solutions and gels-recent results on pectins*, Carbohydr. Polym. 2 (1982), p. 254.
[14] W.G.T. Willats et al., *Modulation of the degree and pattern of methylesterification of pectic homogalacturonan in plant cell walls*, J. Biol. Chem. 276 (2001), p. 19404.
[15] E. Onsoyen, *Commercial applications of alginates*, Carbohydr. Eur. 14 (1996), p. 26.
[16] D.A. Rees and J.W.B. Samuel, *The structure of alginic acid. Part VI. Minor features and structure variations*, J. Chem. Soc. C (1967), p. 2295.
[17] C.K. Siew and P.A. Williams, *New insights into the mechanism of gelation of alginate and pectin: charge annihilation and reversal mechainsm*, Biomacromolecules 6 (2005), p. 963.
[18] A. Heyraud et al., *Crystallographic data on bacterial (1 → 4)-β-D-glucuronan*, Carbohydr. Res. 258 (1994), p. 275.
[19] I. Braccini, A. Heyraud, and S. Péerez, *Three-dimensional features of the bacterial polysaccharide*, Biopolymers 45 (1998), p. 165.
[20] L. Dantas et al., *Physicochemical properties of exogel exocellular β(1-4)-D-glucuronan from* Rhizobium meliloti *strain M5N1 C.S (NCIMB 40472)*, Carbohydr. Polym. 24 (1994), p. 185.
[21] G.A. De Ruiter et al., *Isolation and characterization of β(1-4)-D-glucuronans from extracellular polysaccharides of moulds belonging to Mucorales*, Carb. Polym. 18 (1992), p. 1.
[22] A. Heyraud et al., *Structural characterization and rheological properties of an extracellular glucuronan produced by a* Rhizobiummeliloti *M5N1 mutant strain*, Carb. Res. 240 (1993), p. 71.
[23] R.H. Walter, Polysaccharide association structures in food, Marcel Dekker, Inc. (1998).
[24] A. Shilpa, S.S. Agrawal, and A.R. Ray, *Controlled delivery of drugs from alginate matrix*, J. Macromol. Sci. C. 43 (2003), p. 187.
[25] G. Skjak-Braek and T. Espevik, *Application of alginate gels in biotechnology and biomedicine*, Carbohydr. Eur. 14 (1996), p. 19.
[26] K.I. Draget, G. Skjaek-Braek, and O. Smirdsrod, *Alginate based new materials*, Int. J. Biol. Macromol. 21 (1997), p. 45.
[27] A.K. Anal and H. Singh, *Recent advances in microencapsulation of probiotics for industrial applications and target delivery*, Trends in Food Sci. Tech. 18 (2007), p. 240.
[28] T.A. Davis, B. Volesky, and A. Mucci, *A review of the biochemistry of heavy metal biosorption by brown algae*, Water Res. 37 (2003), p. 4311.
[29] E.R. Morris et al., *Chiropractical and stoichiometric evidence of a specific, primary dimerisation process in alginate gelation*, Carbohydr. Res. 66 (1978), p. 145.
[30] J.-F. Thibault and M. Rinaudo, *Chain association of pectic molecules during calcium-induced gelation*, Biopolymers 25 (1986), p. 455.
[31] C.W. Tibbits, A.J. MacDougall, and S.G. Ring, *Calcium binding and swelling behaviour of a high methoxyl pectin gel*, Carbohydr. Res. 310 (1998), p. 101.
[32] G.T. Grant, E.R. Morris, D.A. Rees, P.J.C. Smith, and D. Thom, *Biological interactions between polysaccharides and divalent cations: the egg-box model*, FEBS. Lett. 32 (1973), p. 195.
[33] M.C. Jarvis and D.C. Apperley, *Chain conformation in concentrated pectic gels: evidence from ^{13}C NMR*, Carbohydr. Res. 275 (1995), p. 131.
[34] B.T. Stokke et al., *Small-angle X-ray scattering and rheological characterization of alginate gels. 1. Ca-alginate gels*, Macromolecules 33 (2000), p. 1853.
[35] I. Braccini and S. Pérez, *Molecular basis of Ca^{2+}-induced gelation in alginates and pectins: the egg-box model revisited*, Biomacromolecules 2 (2001), p. 1089.
[36] E.R. Morris et al., *Conformations and interactions of pectins I: polymorphism between gel and solid states of calcium polygalacturonate*, J. Mol. Biol. 155 (1982), p. 507.
[37] Y. Fang et al., *Multiple steps and critical behaviors of the binding of calcium to Alginate*, J. Phys. Chem. B 111 (2007), p. 2456.

[38] E.D.T. Atkins, W. Mackie, and E.E. Smolko, *Crystalline structures of alginic acids*, Nature 225 (1970), p. 626.

[39] E.D.T. Atkins, W. Mackie, K.D. Parker, and E.E. Smolko, *Crystaline structures of poly-D-mannuronic and poly-L-guluronic acids*, Polym. Lett. 9 (1971), p. 311.

[40] E.D.T. Atkins et al., *Structural components of alginic acid II: the crystalline structure of poly-L-guluronic acid. Results of X-ray diffraction and polarized infrared studies*, Biopolymers 12 (1973), p. 1879.

[41] P. Sikorski, F. Mo, G. Skjaek-Braek, and B.T. Stokke, *Evidence for egg-box-compatible interactions in calcium-alginate gels from fiber X-ray diffraction*, Biomacromolecules 8 (2007), p. 2098.

[42] S. Arnott et al., *Lessons for today and tomorrow from yesterday – the structure of alginic acid*, Fibre Diffr. Rev. 9 (2000), p. 44.

[43] W. Mackie, *Conformations of crystalline alginic acids and their salts*, Biochem. J. 125 (1971), p. 89.

[44] M.L. Dheu-Andries and S. Pérez, *Geometrical features of calcium-carbohydrate interactions*, Carbohydr. Res. 124 (1983), p. 324.

[45] I. Donati et al., *Skjaek-Braek new hypothesis on the role of alternating sequences in calcium-alginate gels*, Biomacromolecules 6 (2005), p. 1031.

[46] Y. Yuguchi et al., *Small-angle X-ray scattering and rheological characterization of alginate gels. 2: time-resolved studies on ionotropic gels*, J. Mol. Struct. 554 (2000), p. 21.

[47] L. Li, Y. Fang, R. Vreeker, and I. Appelquist, *Reexamining the egg-box model in calcium-Alginate gels with X-ray diffraction*, Biomacromolecules 8 (2007), p. 464.

[48] M.D. Walkinshaw and S. Arnott, *Conformations and interactions of pectins I. X-ray diffraction analyses of sodium pectate in neutral and acidified form*, J. Mol. Biol. 153 (1981), p. 1055.

[49] I. Braccini, M.A. Rodriguez-Carvajal, and S. Péez, *Chain–chain interactions for methyl polygalacturonate: models for high methyl-esterified pectin junction zones*, Biomacromolecules 6 (2005), p. 1322.

[50] E.D.T. Atkins, H.H. Nieduszynski, W. Mackie, K.D. Parker, and E.E. Smolko, *Structural components of alginic acid I. The crystalline structure of poly-β-D-mannuronic acid. Results of X-ray diffraction and polarized infrared studies*, Biopolymers 12 (1973), p. 1865.

[51] I. Braccini, R.P. Grasso, and S. Péez, *Conformational and configurational features of acidic polysaccharides and their interactions with calcium ions: a molecular modeling investigation*, Carbohydr. Res. 317 (1999), p. 119.

[52] E. Frei and R.D. Preston, *Variants in the structural polysaccharides of algal cell walls*, Nature 196 (1961), p. 130.

[53] B. Boutherin, K. Mazeau, and I. Tvaroska, *Conformational statistics of pectin substances in solution by a Metropolis Monte Carlo*, Carbohydr. Polym. 31 (1997), p. 1.

[54] V.L. Larwood, B.J. Howlin, and G.A. Webb, *Solvation effects on the conformational behaviour of gellation and calcium ion binding to gellan double helices*, J. Mol. Model. 2 (1996), p. 175.

[55] S. Pérez et al., *Modeling polysaccharides: present status and challenges*, J. Mol. Graphics 14 (1996), p. 307.

[56] B. Manunza, S. Deiana, and C. Gessa, *Molecular dynamics study of Ca-polygalacturonate clusters*, J. Mol. Struc. (Theochem) 368 (1996), p. 27.

[57] B. Manunza et al., *A molecular dynamics investigation on the occurrence of helices in polygalacturonic acid*, J. Mol. Struct. (Theochem) 419 (1997), p. 169.

[58] B. Manunza et al., *Molecular dynamics study of polygalacturonic acid chains in aqueous solution*, Carbohydr. Res. 300 (1997), p. 85.

[59] B. Manunza, S. Deiana, M. Pintore, and C. Gessa, *Interaction of Ca^{2+} and Na^{2+} ions with polygalacturonate chains: a molecular dynamics study*, Glycoconjugate J. 15 (1998), p. 297.

[60] T.D. Perry, R.T. Cygan, and R. Mitchell, *Molecular models of alginic acid: Interactions with calcium ions and calcite surfaces*, Geoch. et Cosm. Act. 70 (2006), p. 3508.

[61] N.L. Allinger, *Molecular mechanics. The MM3 force field for hydrocarbons.* 1, J. Am. Chem. Soc. 111 (1989), p. 8551.

[62] N.L. Allinger, *Molecular mechanics. The MM3 force field for hydrocarbons.* 2, *vibrational frequencies and thermodynamics*, J. Am. Chem. Soc. 111 (1989), p. 8566.

[63] N.L. Allinger, *Molecular mechanics. The MM3 force field for hydrocarbons.* 3, *the van der Waals' potentials and crystal data for aliphatic and aromatic hydrocarbons*, J. Am. Chem. Soc. 111 (1989), p. 8576.

[64] P.J. Goodford, *A computational procedure for determining energetically favorable binding sites on biologically important macromolecules*, J. Med. Chem. 28 (1985), p. 849.

[65] I. Donati, A. Cesaro, and S. Paoletti, *Specific interactions versus counterion condensation.* 1, *nongelling ions/polyuronate systems*, Biomacromolecules 7 (2006), p. 281.

[66] I. Donati et al., *Specific interactions versus counterion condensation.* 2, *theoretical treatment within the counterion condensation theory*, Biomacromolecules 7 (2006), p. 1587.

[67] I. Donati, J.C. Benegas, and S. Paoletti, *Polyelectrolyte study of the calcium-induced chain association of pectate*, Biomacromolecules 7 (2006), p. 3439.

[68] R. Noto et al., *Role of charges and solvent on the conformational properties of poly (galacturonic acid) chains: a molecular dynamics study*, Biomacromolecules 6 (2005), p. 2555.

[69] W.F. van Gunsteren et al., *Biomolecular simulation: the GROMOS96 manual and user guide*, Verlag der Fachvereine, Zürich (1996), p. 1.

[70] W.R.P. Scott, W.F. van Gunsteren et al., *The GROMOS biomolecular simulation program package*, J. Phys. Chem. A 103 (1999), p. 3596.

[71] L.D. Schuler and W.F. van Gunsteren, *On the choice of dihedral angle potential energy functions for n-alkanes*, Mol. Simul. 25 (2000), p. 301.

[72] L.D. Schüler, X. Daura, and W.F. van Gunsteren, *An improved GROMOS96 force field for aliphatic hydrocarbons in the condensed phase*, J. Comput. Chem. 22 (2001), p. 1205.

[73] I. Chandrasekhar et al., *A consistent potential energy parameter set for lipids: dipalmitoylphosphatidylcholine as a benchmark of the GROMOS96 45A3 force field*, Eur. Biophys. J. 32 (2003), p. 67.

[74] T.A. Soares et al., *An improved nucleic-acid parameter set for the GROMOS force field*, J. Comput. Chem. 26 (2005), p. 725.

[75] U. Börjesson and P.H. Hünenberger, *pH-dependent stability of a decalysine α-helix studied by explicit-solvent moleculardynamics simulations at constant pH*, J. Phys. Chem. B 108 (2004), p. 13551.

[76] R.D. Lins and P.H. Hünenberger, *A new GROMOS force field for hexopyranose-based carbohydrates*, J. Comput. Chem. 26 (2005), p. 1400.

[77] C.S. Pereira et al., *Conformational and dynamical properties of disaccharides in water: a molecular dynamics study*, Biophys. J. 90 (2006), p. 4337.

[78] V. Kräutler, M. Müller, and P. Hünenberger, *Conformation, dynamics, solvation and relative stabilities of selected beta-hexopyranoses in water: a molecular dynamics study with the GROMOS 45A4 force field*, Carbohydrate Res. 342 (2007), p. 2097.

[79] H.J.C. Berendsen et al., *Interaction models for water in relation to protein hydration*, In Intermolecular Forces, E. Pullman, ed., Reidel, Dordrecht, The Netherlands, 1981, pp. 331–342.

[80] R.W. Hockney, *The potential calculation and some applications*, Methods Comput. Phys. 9 (1970), p. 136.

[81] J.-P. Ryckaert, G. Ciccotti, and H.J.C. Berendsen, *Numerical integration of the Cartesian equations of motion of a system with constraints: molecular dynamics of* n-*alkanes*, J. Comput. Phys. 23 (1977), p. 327.

[82] H.J.C. Berendsen et al., *Molecular dynamics with coupling to an external bath*, J. Chem. Phys. 81 (1984), p. 3684.

[83] W.F. van Gunsteren and H.J.C. Berendsen, *Computer simulation of molecular dynamics: methodology, applications and perspectives in chemistry*, Angew. Chem. Int. Ed. Engl. 29 (1990), p. 992.

[84] T.N. Heinz, W.F. van Gunsteren, and P.H. Hünenberger, *Comparison of four methods to compute the dielectric permittivity of liquids from molecular dynamics simulations*, J. Chem. Phys. 115 (2001), p. 1125.

[85] D. Kony et al., *Explicit-solvent molecular dynamics simulations of the polysaccharide schizophyllan in water*, Biophys. J. 93 (2007), p. 442.
[86] B.T. Stokke et al., *The molecular size and shape of xanthan, xylinan, bronchial mucin, alginate, and amylose as revealed by electron microscopy*, Carbohydr. Res. 160 (1987), p. 13.
[87] B.T. Stokke and D.A. Brant, *The reliability of wormlike polysaccharide chain dimensions estimated from electron micrographs*, Biopolymers 30 (1990), p. 1161.
[88] M. Dentini et al., *Comparative studies on solution characteristics of mannuronan epimerized by C-5 epimerases*, Carbohydr. Polym. 59 (2005), p. 489.
[89] S. Cros et al., *Solution conformations of pectin polysaccharides: determination of chain characteristics by small angle neutron scattering, viscometry, and molecular modeling*, Biopolymers 39 (1996), p. 339.
[90] I.G. Plashchina et al., *Structural studies of the solutions of anionic polysaccharides. IV. Study of pectin solutions by light-scattering*, Cerbohydr. Polym. 5 (1985), p. 159.
[91] K.Y. Lee, K.H. Bouhadur, and D.J. Mooney, *Evaluation of chain stiffness of partially oxidized polyguluronate*, Biomacromolecules 3 (2002), p. 1129.
[92] G. Maurstad, S. Danielsen, and B.T. Stokke, *Analysis of compacted semiflexible polyanions visualized by atomic force microscopy:Influence of chain stiffness on the morfologies of polyelectrolyte complexes*, J. Phys. Chem. B 107 (2003), p. 8172.
[93] Insight II Molecular Modelling Package, *Molecular Simulations Inc.* (2000).
[94] P. Karlson, H.B. Dixon, and C. Liebecq, *Symbols for specifying the conformation of the polysaccharide chains*, Eur. J. Biochem. 131 (1983), p. 5.
[95] S. Pérez and C. Vergelati, *Unified representation of helical parameters: application to polysaccharides*, Biopolymers 24 (1985), p. 1809.
[96] J. Sugiyama, R. Vuong, and H. Chanzy, *Electron diffraction study on the two crystalline phases occuring in native cellulose from an algal cell wall*, Macromolecules 24 (1991), p. 4168.
[97] R.U. Lemieux and S. Koto, *The conformational properties of the glycosidic linkages*, Tetrahedron 30 (1974), p. 1933.
[98] S. Pérez and R.H. Marchessault, *The exo-anomeric effect: experimental evidence from crystal structures*, Carbohydr. Res. 65 (1978), p. 114.
[99] P.P. Graczyk and M. Mikolajczyk, *Anomeric effect. Origin and consequences*, Topics Stereochem. 21 (1994), p. 159.
[100] H. Thogersen et al., *Further justification for the* exo-*anomeric effect. Conformational analysis based on nuclear magnetic resonance spectroscopy of oligosaccharides*, Can. J. Chem. 60 (1982), p. 44.
[101] I. Tvaroška and J.P. Carver, *The anomeric and* exo-*anomeric effects of a hydroxyl group and the stereochemistry of the hemiacetal linkage*, Carbohydr. Res. 309 (1998), p. 1.
[102] M.A. Kastenholz and P.H. Hünenberger, *Computation of methodology-independent ionic solvation free energies from molecular simulations:* I. *The electrostatic potential in molecular liquids*, J. Chem. Phys. (2006), p. 124.
[103] M.A. Kastenholz and P.H. Hünenberger, *Computation of methodology-independent ionic solvation free energies from molecular simulations:* II. *the hydration free energy of the sodium cation*, J. Chem. Phys 124 (2006), on-line (DOI: 10.1063/1.2201698).
[104] R.C. Weast, *Handbook of chemistry and physics*, The Chemical Rubber Co., pE-49 (1972).
[105] P.I.W. de Bakker, P.H. Hünenberger, and J.A. McCammon, *Molecular dynamics simulations of the hyperthermophilic protein Sac7d from* Sulfolobus acidocaldaricus*: contribution of salt bridges to thermostability*, J. Mol. Biol. 285 (1999), p. 1811.
[106] K.H. Gardner and J. Blackwell, *The structure of native cellulose*, Biopolymers 13 (1974), p. 1975.
[107] A. Imberty and S. Péerez, *A revisit to the three-dimensional structure of B-type starch*, Biopolymers 25 (1988), p. 1205.
[108] A. Imberty et al., *The double-helical nature of the crystalline part of A-starch*, J. Mol. Biol. 201 (1988), p. 365.